Inorganic Chemistry

Article

pubs.acs.org/IC

Synthesis and Isomeric Analysis of Ru^{II} Complexes Bearing Pentadentate Scaffolds

Marcos Gil-Sepulcre,[†] Jordan C. Axelson,[‡] Joan Aguiló,[†] Lluís Solà-Hernández,[†] Laia Francàs,[§] Albert Poater,[∥] Lluís Blancafort,[∥] Jordi Benet-Buchholz,[§] Gonzalo Guirado,[†] Lluís Escriche,[†] Antoni Llobet,[†,§] Roger Bofill,*[,†] and Xavier Sala*[,†]

[†]Departament de Química, Facultat de Ciències, Universitat Autònoma de Barcelona, 08193 Cerdanyola del Vallès, Barcelona, Catalonia, Spain

[‡]Department of Chemistry, University of California, Berkeley, California 94720, United States

[§]Institute of Chemical Research of Catalonia, Barcelona Institute of Science and Technology, Av. Països Catalans 16, 43007 Tarragona, Catalonia, Spain

[∥]Institut de Química Computacional i Catàlisi and Departament de Química, Facultat de Ciències, Universitat de Girona, 17003 Girona, Catalonia, Spain

Supporting Information

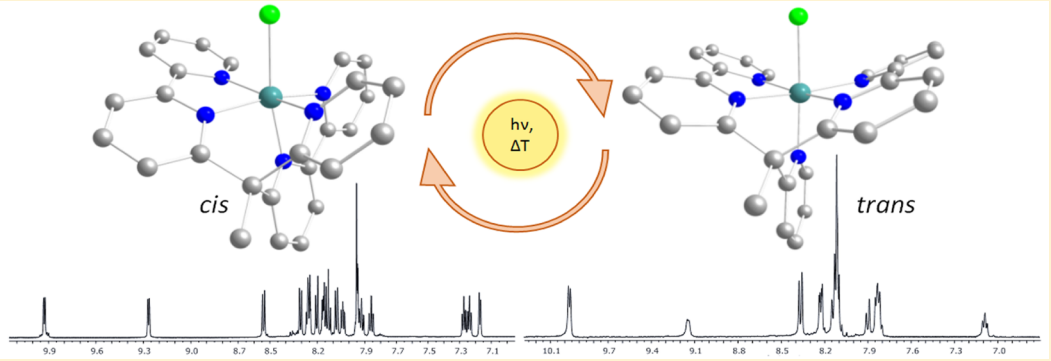

ABSTRACT: A Ru^{II}-pentadentate polypyridyl complex $[Ru^{II}(\kappa\text{-}N^5\text{-bpy2PYMe})Cl]^+$ ($\mathbf{1}^+$, bpy2PYMe = 1-(2-pyridyl)-1,1-bis(6−2,2′-bipyridyl)ethane) and its aqua derivative $[Ru^{II}(\kappa\text{-}N^5\text{-bpy2PYMe})(H_2O)]^{2+}$ ($\mathbf{2}^{2+}$) were synthesized and characterized by experimental and computational methods. In MeOH, $\mathbf{1}^+$ exists as two isomers in different proportions, cis (70%) and trans (30%), which are interconverted under thermal and photochemical conditions by a sequence of processes: chlorido decoordination, decoordination/recoordination of a pyridyl group, and chlorido recoordination. Under oxidative conditions in dichloromethane, *trans*-$\mathbf{1}^{2+}$ generates a $[Ru^{III}(\kappa\text{-}N^4\text{-bpy2PYMe})Cl_2]^+$ intermediate after the exchange of a pyridyl ligand by a Cl^- counterion, which explains the trans/cis isomerization observed when the system is taken back to Ru(II). On the contrary, *cis*-$\mathbf{1}^{2+}$ is in direct equilibrium with *trans*-$\mathbf{1}^{2+}$, with absence of the κ-N^4-bis-chlorido Ru^{III}-intermediate. All these equilibria were modeled by density functional theory calculations. Interestingly, the aqua derivative is obtained as a pure *trans*-$[Ru^{II}(\kappa\text{-}N^5\text{-bpy2PYMe})(H_2O)]^{2+}$ isomer (*trans*-$\mathbf{2}^{2+}$), while the addition of a methyl substituent to a single bpy of the pentadentate ligand leads to the formation of a single cis isomer for both chlorido and aqua derivatives $[Ru^{II}(\kappa\text{-}N^5\text{-bpy(bpyMe)PYMe})Cl]^+$ ($\mathbf{3}^+$) and $[Ru^{II}(\kappa\text{-}N^5\text{-bpy(bpyMe)PYMe})(H_2O)]^{2+}$ ($\mathbf{4}^{2+}$) due to the steric constraints imposed by the modified ligand. This system was also structurally and electrochemically compared to the previously reported $[Ru^{II}(PY5Me_2)X]^{n+}$ system (X = Cl, n = 1 ($\mathbf{5}^+$); X = H_2O, n = 2 ($\mathbf{6}^{2+}$)), which also contains a κ-N^5−Ru^{II} coordination environment, and to the newly synthesized $[Ru^{II}(PY4Im)X]^{n+}$ complexes (X = Cl, n = 1 ($\mathbf{7}^+$); X = H_2O, n = 2 ($\mathbf{8}^{2+}$)), which possess an electron-rich κ-N^4C−Ru^{II} site due to the replacement of a pyridyl group by an imidazolic carbene.

INTRODUCTION

Transition-metal complexes containing polypyridyl ligands have been extensively used in catalytic oxidation systems due to their stability and synthetic versatility.[1] Among these, Ru-aqua polypyridyl complexes are particularly interesting because of both their easily accessible high oxidation states through proton-coupled electron transfer (PCET) processes and the inertness of the polypyridyl ligands bonded to the Ru metal center.[2]

Pentadentate ligands that coordinate metals in a square pyramidal fashion are able to both enforce an octahedral

Received: July 29, 2016

DOI: 10.1021/acs.inorgchem.6b01755
Inorg. Chem. XXXX, XXX, XXX−XXX

geometry around the metal center as well as restrict the metal substitution chemistry to a single coordination site.[3] An archetypical example is the $PY5R_2$ family (PY = pyridine, R = H, Me, OH, OMe, etc., Chart 1), which usually binds the metal

Chart 1. Schematic Drawing of the Ligands Discussed in This Work

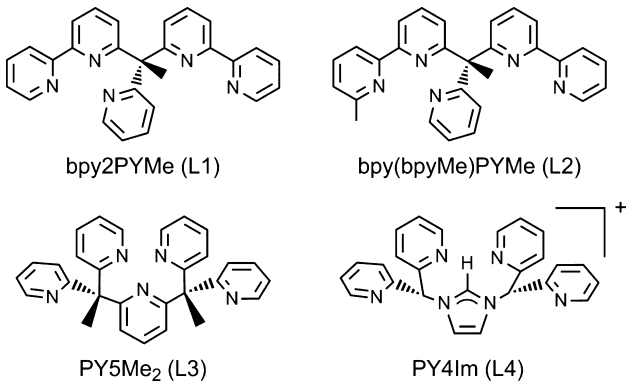

ion through one axial and four equatorial positions.[4] Recently, several works have emerged taking advantage of the interesting properties of this scaffold. For instance, Berlinguette et al. have reported the first tetravalent Co complex stabilized by PCET processes by employing the $PY5R_2$ ligand (R = H).[5] This pentadentate ligand ensures (a) one single free coordination site in an octahedral type of geometry to accommodate the aqua ligand, thus allowing PCET processes, (b) a rugged coordination environment nonsusceptible to oxidative decomposition, and (c) the stabilization of the coordination site trans to the M−O bond, preventing in consequence decomposition via ligand dissociation. Other examples of the $PY5R_2$ family include the $PY5Me_2$ ligand (R = Me),[6] whose Ru^{III}−OH complex was recently reported by Kojima et al. to oxidize substrates such as hydroquinones in water.[7] In addition, $PY5Me_2$-related compounds containing Co(II)[8] and Mo(II)[9] have been proven to be active in electrocatalytic water reduction. Also, in 2010, Long and co-workers reported a series of first-row metal complexes containing the PY4Im ligand, in which the axial pyridine of the $PY5R_2$ scaffold was replaced by a N-heterocyclic carbene (NHC) moiety.[10] Finally, the same group reported in 2013 a series of first-row metal complexes containing the related pentapyridyl ligand bpy2PYMe, which in the case of Co(II) has been shown to be an active catalyst for the proton reduction reaction.[6b,11]

An important issue to be considered during redox catalysis employing polypyridyl transition-metal complexes is the potential presence of several isomers due to the flexibility of the polydentate ligand, which can hamper a rational analysis of their behavior.[12] Furthermore, it is also fundamental to assess the stability of a given isomer when the central metal ion experiences the gain or loss of an electron. Within this context, we present the synthesis and isomeric analysis by spectroscopic, electrochemical, and theoretical (density functional theory (DFT)) methods of two Ru(II) complexes bearing 1-(2-pyridyl)-1,1-bis(6−2,2′-bipyridyl)ethane ligand scaffolds (L1 and L2 in Chart 1) and the comparison of their structural and electronic properties with those of related Ru(II) complexes containing the pentadentate ligands L3 and L4 (Chart 1).

RESULTS AND DISCUSSION

Synthesis and Characterization of 1(Cl), $2(PF_6)_2$, 3(Cl) and $4(PF_6)_2$. For the synthesis of bpy2PYMe (L1), the two-step procedure reported by Long and co-workers[11] involved reacting 2-ethylpyridine with MeLi and 6-bromo-2,2′-bipyridine and mixing the isolated intermediate with BuLi and another equivalent of 6-bromo-2,2-bipyridine. However, in this study the route was simplified to a one-pot reaction of 2-ethylpyridine with lithium diisopropylamide (LDA) and 6-bromo-2,2′-bipyridine, obtaining L1 as a yellow oil in 70% yield (a detailed description of the synthesis can be found in the Supporting Information). The synthetic strategy followed for the preparation of the respective chlorido and aqua complexes **1(Cl)** and $\mathbf{2(PF_6)_2}$ is depicted in Scheme 1 and in the Experimental Section.

Scheme 1. Synthetic Pathway for the Preparation of the Chlorido Complexes 1^+ and 3^+ and the Aqua Complexes 2^{2+} and 4^{2+}

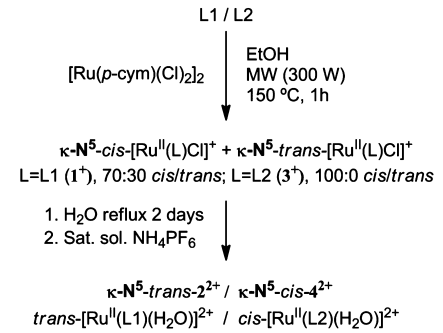

For the synthesis of the chlorido complex $\mathbf{1}^+$, the ^{1}H NMR spectrum of the reaction mixture in ethanolic solution showed the presence of two compounds, which could be separated by fractionated precipitation through sequential exposure to ethanol followed by dichloromethane (DCM; see the Experimental Section for further details). With this method, two pure isomers were obtained, which were called *trans*-$\mathbf{1}^+$ and *cis*-$\mathbf{1}^+$, respectively, depending on whether the pyridyl moiety is positioned trans or cis with respect to the Cl^- ligand (Scheme 1 and Figure 1).

The experimentally obtained cis/trans ratio is ∼70:30, and both individual compounds were characterized by NMR (Figure 2 and Figures S1 and S2), UV−vis spectroscopy (Figure S3), and electrospray ionization time-of-flight (ESI-TOF) and matrix-assisted laser desorption/ionization time-of-flight mass spectrometry (MALDI-TOF MS; Figure S4).

The higher symmetry of the trans isomer, which belongs to the C_s point group, compared to the C_1 point group of the cis isomer, can be confirmed in the NMR spectra; whereas the former only shows 12 ^{1}H and 17 ^{13}C resonances (Figure 2a and Figure S1a), the latter displays 19 ^{1}H and 27 ^{13}C resonances (Figure 2b and Figure S2a). The unequivocal assignment of the respective cis and trans isomers is also clear when observing the integrals of the downfield doublets corresponding to H19, H1, and H16 (1:1:1) and H1 and H12 (2:1), respectively.

Complexes *cis*-$\mathbf{1}^+$ and *trans*-$\mathbf{1}^+$ are both stable in a DCM solution in darkness at room temperature (RT). However, at 0 °C in the presence of light (100 W incandescent white light bulb) *trans*-$\mathbf{1}^+$ is partially converted into *cis*-$\mathbf{1}^+$ as monitored by NMR. In sharp contrast, *cis*-$\mathbf{1}^+$ remains stable in DCM under

DOI: 10.1021/acs.inorgchem.6b01755
Inorg. Chem. XXXX, XXX, XXX−XXX

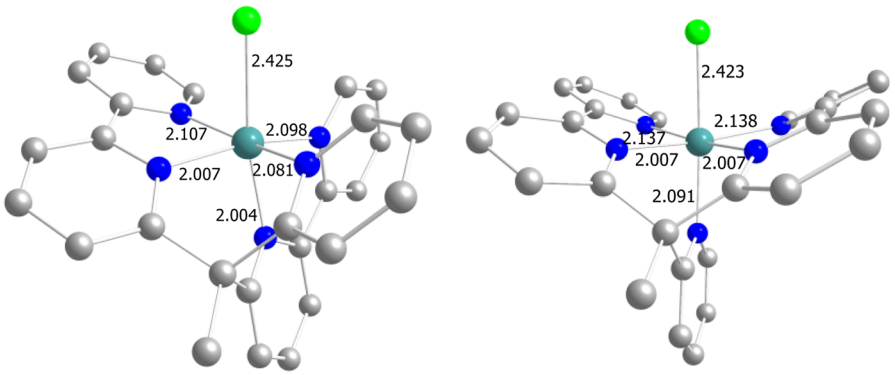

Figure 1. Plot of the DFT-calculated structures of *cis*-$\mathbf{1}^+$ (left) and *trans*-$\mathbf{1}^+$ (right). Atom color code: blue, nitrogen; light green, chlorine; dark green, ruthenium; light gray, carbon. All Ru−X calculated distances (X = Cl, N) are shown in angstroms. Hydrogen atoms were omitted for clarity.

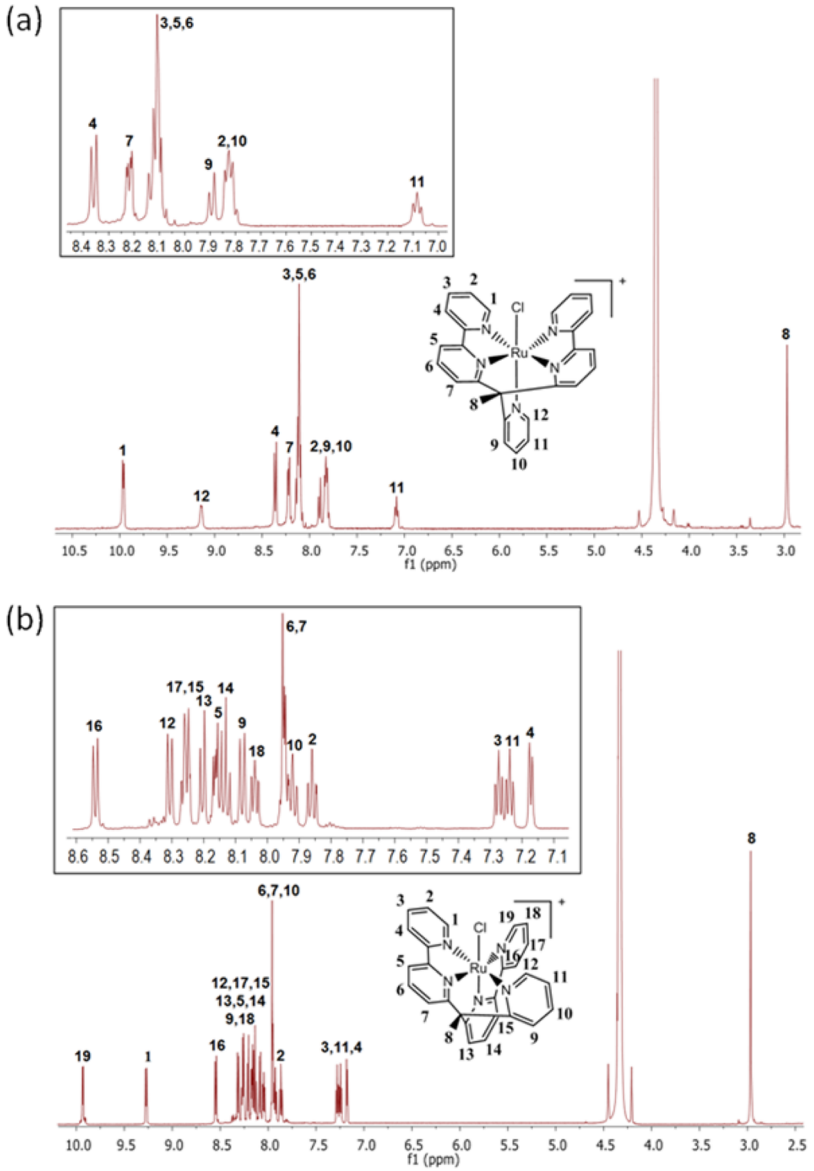

Figure 2. ^{1}H NMR spectra including the assignment of signals for *trans*-$\mathbf{1}^+$ (400 MHz, 298 K, $MeNO_2$-d_3) (a) and *cis*-$\mathbf{1}^+$ (600 MHz, 298 K, $MeNO_2$-d_3) (b). An enlargement of the aromatic region is shown in the insets.

irradiation. Interestingly, the behavior of both isomers is completely different in MeOH. In this case both isomers are interconverted under irradiation at 0 °C and under heating (RT or 50 °C) in darkness, with faster interconversion rates observed for the photoinduced case. For example, under irradiation at 0 °C pure *cis*-$\mathbf{1}^+$ is converted into a *cis*-$\mathbf{1}^+$/*trans*-$\mathbf{1}^+$

DOI: 10.1021/acs.inorgchem.6b01755
Inorg. Chem. XXXX, XXX, XXX−XXX

(73:15) mixture, and pure *trans*-$\mathbf{1}^+$ is converted into a *cis*-$\mathbf{1}^+$/*trans*-$\mathbf{1}^+$ (63:19) mixture within 30 h (Figure S5). Furthermore, an additional minor species was detected by NMR (12% abundance for the former case and 18% for the latter), in which at least one MeOH solvent molecule is coordinated to the Ru ion.

To obtain additional information regarding the potential mechanism of isomerization between *trans*-$\mathbf{1}^+$ and *cis*-$\mathbf{1}^+$, DFT calculations[13] in MeOH and DCM were performed (Figure 3).

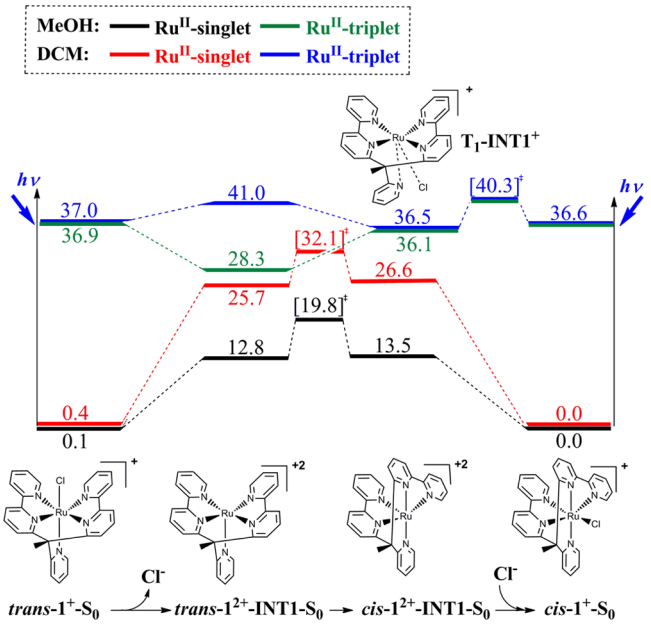

Figure 3. Energy diagram (B3LYPd3/TZVP-D95+ ~ sdd// B3LYPd3/SVP ~ sdd) for the thermal and photoinduced isomerization processes for $\mathbf{1}^+$ in MeOH and DCM. Red curve denotes the singlet spin surface, and blue curve denotes the triplet spin surface in DCM, whereas black and green curves denote the singlet and triplet spin surfaces in MeOH, respectively. All Gibbs energies are calculated relative to *cis*-$\mathbf{1}^+$ and are reported in kcal/mol (transition-state energies in brackets). S_0 = ground state, T_1 = first excited triplet state.

In both solvents, the calculations tend to show a slightly higher stability of the cis isomer by 0.1 kcal/mol in MeOH and by 0.4 kcal/mol in DCM. The isomerization may be understood as a stepwise equilibrium involving three steps: (1) decoordination of the chlorido ligand, (2) isomerization of one pyridyl group in the decoordinated species, and (3) recoordination of the chloride ion (see Figure 3). Light-induced Ru−Cl bond breakage should not be surprising, since breakage of Ru−X bonds (e.g., X = N, S, O) in Ru(II)-polypyridyl complexes upon light irradiation has been previously described elsewhere.[14] Interestingly, in our case the DFT calculations determined that reaching the equilibrium starting from a single form depends on the polarity of the solvent, as has been experimentally observed. In MeOH, the chlorido decoordination step from the *trans*-$\mathbf{1}^+$ and *cis*-$\mathbf{1}^+$ forms costs 12.7 and 13.5 kcal/mol, respectively, and the barrier involving the ligand isomerization step is 19.7 kcal/mol. Therefore, the isomerization is energetically possible in MeOH at RT, and the equilibrium between the cis and trans forms can be established. In contrast, in DCM the decoordination, isomerization, and decoordination sequence has a barrier of 32.1 kcal/mol due to the lower polarity of the solvent, which disfavors the separation of charges that occurs during this process. Although there is a concerted transition state linking the two isomers of $\mathbf{1}^+$ in DCM, this path is not viable energetically, because it has a barrier of 37.4 kcal/mol relative to *trans*-$\mathbf{1}^+$ (see coordinate data sets and absolute energy for DFT-optimized complexes in the Supporting Information). Thus, the cis and trans isomers are kinetically trapped under these conditions, and no isomerization occurs at RT.

The cis-trans isomerization in the photoexcited triplet state also follows the chlorido decoordination/recoordination mechanism according to the calculations, which are in agreement with the experimentally observed behavior (Figure 3). Under these conditions, isomerization from the trans to the cis isomer occurs in both solvents. The calculations show that the chlorido decoordination step is exothermic in MeOH by 8.6 kcal/mol, while it is only slightly endothermic in DCM (by 4.0 kcal/mol). The different endothermicity of the reaction in the ground and excited state explains why *trans*-$\mathbf{1}^+$ is stable in DCM in the dark but not under irradiation. The situation is different for the triplet-state isomerization in the cis to trans direction, which occurs only in MeOH. The decoordination reaction starting from *cis*-$\mathbf{1}^+$ follows a stepwise mechanism that goes through an intermediate, $\mathbf{T_1}$-**INT-1**$^+$, where the chlorine atom is partially dissociated (Ru−Cl distance of 4.0 Å) and the ligand has a quasi-trans conformation. The barrier for this step is low in both solvents (3.7 kcal/mol). At $\mathbf{T_1}$-**INT-1**$^+$, the energy gap between the triplet and ground state is small, 5.1 kcal/mol in DCM and 5.6 kcal/mol in MeOH. Therefore, when the molecule is at $\mathbf{T_1}$-**INT-1**$^+$, it can decay from the triplet to the ground state instead of completing the dissociation. In the ground state, this is followed by reassociation of the chloride ion to the complex and regeneration of the *cis*-$\mathbf{1}^+$ species without isomerization. The calculations suggest that this process will be more favorable in DCM, where the energy gap is smaller, and this might explain why the light-induced isomerization from the cis form is suppressed in this solvent but not in MeOH. Such nonadiabatic processes are common in the photoreactivity of transition-metal complexes[15] and organic molecules,[16] and involvement of a singlet/triplet crossing has been previously postulated in the photoisomerization of Ru(II) monoaquo complexes.[17]

The computational results also indicate that the minor species (12−18%) detected in the NMR experiments in MeOH are the trapping products of the decoordinated intermediates. This corresponds to a stepwise replacement of the chlorido ligands by MeOH. The relative energy of the MeOH-coordinated products is 5.2 and 5.9 kcal/mol with respect to *trans*-$\mathbf{1}^+$ and *cis*-$\mathbf{1}^+$, respectively. The alternative structures where MeOH replaces one of the pyridyl ligands instead of a chloride are less favorable energetically; from *trans*-$\mathbf{1}^+$ the cost of dissociating the pyridyl ligand trans to Cl^- (25.0 kcal/mol, Figure S6) is higher than that of the chloride dissociation, and the concerted substitution of the pyridyl ligand by MeOH is 6.4 kcal/mol even higher in energy.

The electrochemical behavior of the *cis*-$\mathbf{1}^+$ and *trans*-$\mathbf{1}^+$ isomers was also studied in DCM, a noncoordinating solvent, at different scan rates (Figure 4).

Typical cyclic voltammograms (CVs) for *trans*-$\mathbf{1}^+$ show a one-electron pseudoreversible wave at 0.829 V versus saturated calomel electrode (SCE).[18] In the corresponding cathodic counter scan and in a second scan a new reversible wave appears at 0.241 V versus SCE, indicating the formation of a new electroactive product through a chemical reaction linked to the Ru^{II}/Ru^{III} electron transfer process (Figure 4a and Figure

DOI: 10.1021/acs.inorgchem.6b01755
Inorg. Chem. XXXX, XXX, XXX−XXX

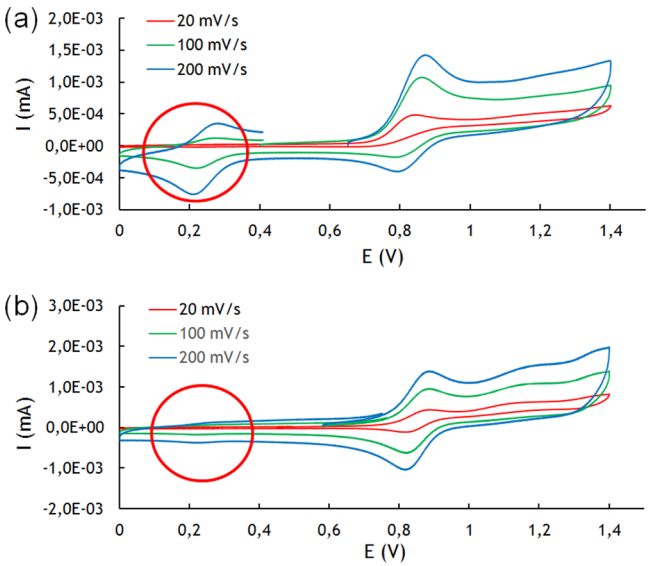

Figure 4. CV for *trans*-$\mathbf{1}^+$ (a) and *cis*-$\mathbf{1}^+$ (b) in DCM + 0.1 M *n*-Bu_4NPF_6 at different scan rates. Glassy carbon electrode is used as working electrode (diameter: 1 mm). The redox potentials are determined vs SCE. Red circle denotes formation of $[Ru^{II/III}(\kappa\text{-}N^4\text{-bpy2PYMe})Cl_2]^{0/+}$ intermediate.

S7, red). A closer look at the CVs reveals that the peak currents are of the same order of magnitude as those expected for a one-electron transfer reaction for a diffusing solution species in DCM.[19] The analysis of the peak current values (and their dependence on concentration and scan rate), the peak potential values (and their dependence on concentration), and the potential width values provide a window into the nature of the electrochemical mechanism and the values of the kinetics constants coupled to the electron transfer. Increasing the concentration of *trans*-$\mathbf{1}^+$ results in increases in the peak current value without significant shifts in the peak potential up 0.5 mM, whereas the anodic peak potential shows a dependence with scan rate (ca. 30 mV), which means that an electrochemical step (E) is followed by a first-order chemical reaction (C), EC mechanism (Figure S8).[19]

In the case of the *cis*-$\mathbf{1}^+$ isomer, a similar electrochemical behavior is observed: a quasi-reversible one-electron oxidation wave appears at 0.851 V, and the same peak detected in solutions of *trans*-$\mathbf{1}^+$ isomer appears again at 0.241 V in the corresponding cathodic counter scan but now with lower associated currents (Figure 4b). The lower cathodic and anodic peak current values obtained for the peak at 0.241 V reflect the higher stability of the oxidized *cis*-$\mathbf{1}^{2+}$ form in comparison with *trans*-$\mathbf{1}^{2+}$ (Figure S7, black).

To determine the nature of the product formed after the first electron transfer of *trans*-$\mathbf{1}^+$, a controlled potential electrolysis (CPE) at 1.2 V versus SCE was performed in darkness. After the passage of 1.0 F per mol of complex, the analysis of the oxidized sample by means of CV shows the formation of the electroactive product at 0.241 V (Figure S9). Interestingly, this species is not formed when exchanging the coordinating Cl^- counterion in $\mathbf{1}^+$ by the noncoordinating PF_6^- ion. The CV of *trans*-$[Ru^{II}(bpy2PYMe)Cl](PF_6)$ in DCM only shows a reversible wave at 0.829 V, with complete absence of the signal of the new species at 0.241 V (Figure S9c). Therefore, the new species must be formed upon coordination of a Cl^- ion to the Ru metal center under oxidative conditions in DCM to generate a $[Ru^{III}(\kappa\text{-}N^4\text{-bpy2PYMe})Cl_2]^+$ species (or **κ-N⁴-bis-Cl⁺**) after the exchange of a pyridyl ligand by a Cl^- counterion. Indeed, this **κ-N⁴-bis-Cl⁺** species shows a Ru^{III}/Ru^{II} potential of 0.241 V versus SCE ($[Ru^{III}(bpy2PYMe)Cl_2]^+/[Ru^{II}(bpy2PYMe)Cl_2]$ redox pair) by CV and has been detected by MALDI-TOF MS after a CPE at 1.2 V for 6 h (7.56 F/mol) of a *trans*-$\mathbf{1}^+$ sample. As can be observed in Figure S4a, the higher intensity of the upper molecular weight peaks compared to the parent *cis*-$\mathbf{1}^+$ and *trans*-$\mathbf{1}^+$ compounds is indicative of the presence of the second Cl^- atom in the bis-chlorido compound, since total loss of one Cl^- ligand and partial loss of the second Cl^- ligand is happening. Interestingly, when oxidizing *trans*-$\mathbf{1}^+$ in darkness in DCM (CPE at 1.2 V for 16 h, 4.15 F/mol) and then reducing it back again (CPE at 0 V for 5 h, 1.62 F/mol), a 70:30 mixture of *cis*-$\mathbf{1}^+$/*trans*-$\mathbf{1}^+$ was obtained according to NMR data (Figure S10), which is the same proportion obtained during the synthesis of $\mathbf{1}^+$ (Scheme 1). Consequently, isomerization can also be achieved in noncoordinating solvents (DCM) by bulk electrolysis. Therefore, the **κ-N⁴-bis-Cl⁺** species formed after oxidation of *trans*-$\mathbf{1}^+$ is in fact an intermediate in the isomerization process that, when reduced back to Ru(II), may exchange either of the two chloride ligands with the dangling N_{pyr} ligand. If the exchanged Cl^- ion is the same as the one that entered during oxidation, the system will return to the original isomer (*trans*-$\mathbf{1}^+$), whereas if the other is lost, the *cis*-$\mathbf{1}^+$ isomer will be formed. It also became apparent that the $[Ru^{II}(\kappa\text{-}N^4\text{-bpy2PYMe})Cl_2]$ intermediate (**κ-N⁴-bis-Cl**) formed upon reduction at potentials lower than 0.241 V is poorly stable, since its detection by MS or NMR has been completely unfruitful.

A detailed analysis of the CV parameters for *trans*-$\mathbf{1}^+$ and *cis*-$\mathbf{1}^+$ at different scan rates allows for the experimental determination of their first-order kinetics constants, 1.6 and 0.02 s^{-1}, respectively, by plotting the anodic peak potential versus log v (where v is scan rate, V s^{-1}) and log[$\mathbf{1}^+$] for both *cis*-$\mathbf{1}^+$ and *trans*-$\mathbf{1}^+$ (Figure S8) according to the following eqs 1 and (2).[19]

$$I_p = 0.446nFSC^\circ\sqrt{\frac{F}{RT}}\sqrt{v}\sqrt{D} \quad (1)$$

$$E_p = E^\circ + 0.78\left(\frac{RT}{F}\right) - \left(\frac{RT}{2F}\right)\ln\left(\frac{RT}{Fkv}\right) \quad (2)$$

From this analysis, it can be deduced that the Ru(III)-species *trans*-$\mathbf{1}^{2+}$ possesses a lower ΔG^0 compared to the *cis*-$\mathbf{1}^{2+}$ isomer. Thus, the bis-chlorido Ru(III)-intermediate (**κ-N⁴-bis-Cl⁺**) is not formed directly after the oxidation of *cis*-$\mathbf{1}^+$ (Figure 4b) but through a previously established equilibrium between *cis*-$\mathbf{1}^{2+}$ and *trans*-$\mathbf{1}^{2+}$ (Scheme 2). Hence, in all cases, departing either from *cis*-$\mathbf{1}^+$ or *trans*-$\mathbf{1}^+$, the Ru(III)-bis chlorido intermediate is only formed after the formation of *trans*-$\mathbf{1}^{2+}$. Finally, the remaining kinetics and thermodynamic parameters were obtained by individually simulating the experimental CVs recorded at 200 mV/s for both *cis*-$\mathbf{1}^+$ and *trans*-$\mathbf{1}^+$ by an iterative mathematical process using the DigiSim 2.0 CV simulator software[20] (Figure S11) assuming the proposed mechanistic model of Scheme 2 (for further details please refer to the Experimental Section).[21] The dramatic differences between the value of the thermodynamic constant K_1 deduced for Ru(III) and those of K_2 and K_3 deduced for Ru(II) between the **κ-N⁴-bis-Cl** and the **κ-N⁵-Cl** species is also consistent with the hard−soft acid−base (HSAB) theory and the charge of the central metal ion. Thus, according to the HSAB principle one

DOI: 10.1021/acs.inorgchem.6b01755
Inorg. Chem. XXXX, XXX, XXX−XXX

Scheme 2. Proposed Isomeric Equilibria and Kinetic Rate Constants (k, in s^{-1}) and Thermodynamic Constants (K, highlighted in boxes) in Dichloromethane under Oxidative and Reductive Conditions of *cis*-1^+ and *trans*-1^+ Complexes

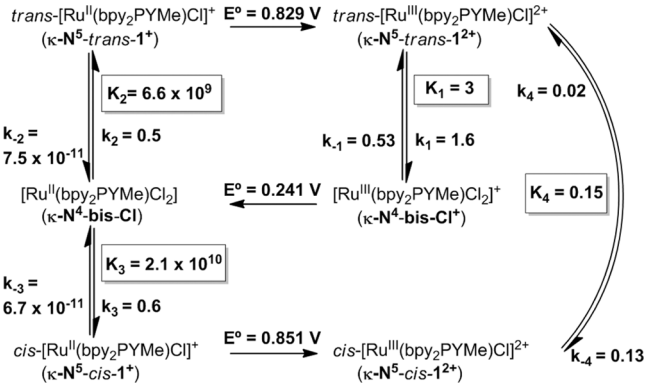

might expect higher affinity of Ru(II) to bind to N-donor ligands compared to a chlorido ligand, whereas for Ru(III) the higher charge on the metal makes it more prone to bind to negatively charged ligands.

To obtain more insight into the electrochemical behavior of $\mathbf{1}^+$, we modeled the formation of the bis-chlorido intermediates **κ-N⁴-bis-Cl** and **κ-N⁴-bis-Cl⁺** species in DCM by DFT calculations (Figure 5). The **κ-N⁴-bis-Cl** species can exist as several possible isomers, of which we characterized the two most likely to be formed from a structural viewpoint. These two isomers are labeled *trans*-1-INT3-S_0 and *cis*-1-INT3-S_0, where the two chlorido ligands are in trans or cis configuration, respectively. We postulate that these isomers are formed from *trans*-$\mathbf{1}^+$ and *cis*-$\mathbf{1}^+$ after decoordination of the single pyridyl ligand and coordination of the chloride counterion. The barriers for pyridyl decoordination are 25.5 and 26.7 kcal/mol, respectively, and the relative energy of the **κ-N⁴-bis-Cl** intermediates INT3 are 9.2 kcal/mol (for trans) and 25.1 kcal/mol (for cis). From the electrochemical measurements, the relative energy of the **κ-N⁴-bis-Cl** intermediate is 14.2 kcal/mol, which suggests that the isomer detected experimentally corresponds to *trans*-INT3, where both chlorido ligands are in axial positions and the electrostatic repulsion between these two ligands is reduced. In Figure 5 we also show a possible isomerization path that interconnects both isomers of INT3. Starting from *trans*-INT3, it involves decoordination of a chlorido ligand to give *trans*-INT4, rotation of one of the bipyridyl ligands, and recoordination of the chloride ion.

With regard to the Ru(III) species, the possible cis−trans isomerization pathway involving chlorido decoordination and recoordination is shown in Figures S12 and S13. The decoordination step from *trans*-$\mathbf{1}^{2+}$ in MeOH and DCM has high barriers of 29.1 and 48.9 kcal/mol, respectively, because of the higher charge on the Ru atom, and probably precludes the occurrence of this mechanism for $\mathbf{1}^{2+}$. In consequence, for Ru(III) the isomerization involving the **κ-N⁴-bis-Cl⁺** inter-

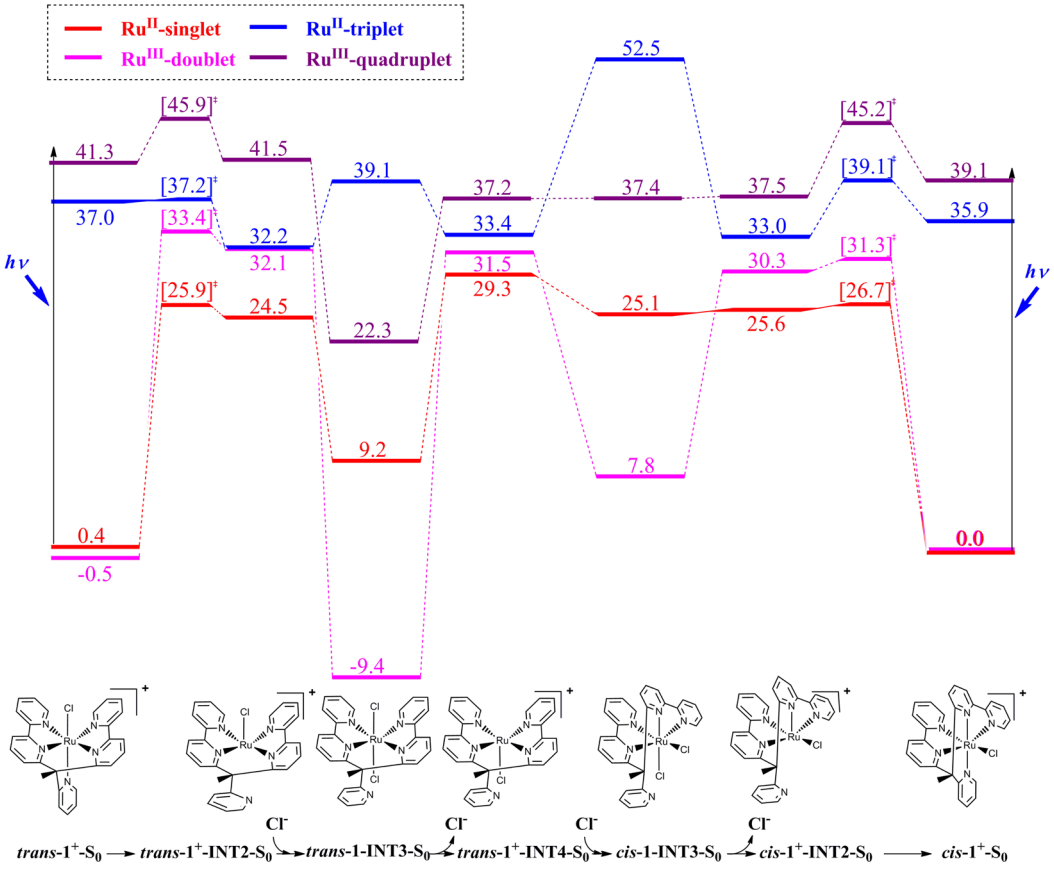

Figure 5. Energy diagram (B3LYPd3/TZVP-D95+ ~ sdd//B3LYPd3/SVP ~ sdd) for the thermal and photoinduced isomerization processes for $\mathbf{1}^+$ and $\mathbf{1}^{2+}$ in DCM in the presence of added chloride ions. Red curve denotes the singlet spin surface, and blue curve denotes the triplet spin surface for Ru^{II}, whereas pink and violet curves denote the doublet and quadruplet spin surfaces for Ru^{III}, respectively. All Gibbs energies are calculated relative to *cis*-$\mathbf{1}^+$ or *cis*-$\mathbf{1}^{2+}$ and are reported in kcal/mol (transition-state energies in brackets). S_0 = ground state.

DOI: 10.1021/acs.inorgchem.6b01755
Inorg. Chem. XXXX, XXX, XXX−XXX

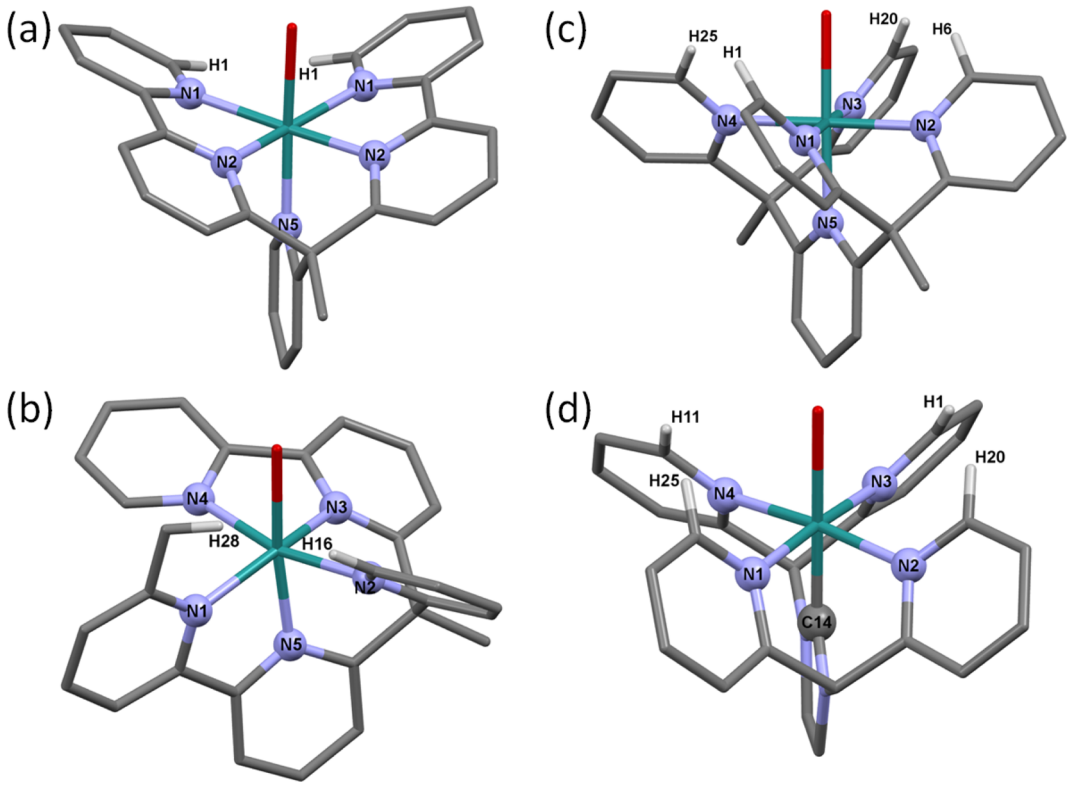

Figure 6. Mercury plot of the X-ray crystal structures of *trans*-$\mathbf{2}^{2+}$ (a), *cis*-$\mathbf{4}^{2+}$ (b), $\mathbf{6}^{2+}$ (c), and $\mathbf{8}^{2+}$ (d). Atom color code: blue, nitrogen; red, oxygen; dark green, ruthenium; light gray, carbon. Only the hydrogen atoms closest to the oxygen atoms are shown in white.

mediate is the more favorable path in DCM, since it involves a maximum barrier of 33.9 kcal/mol (Figure 5) compared to the barrier of 48.9 kcal/mol for the chlorido decoordination (Figure S13).

The corresponding aqua complex $\mathbf{2}^{2+}$ was prepared by stirring an aqueous solution of $\mathbf{1}^{+}$ for 2 d under reflux (Scheme 1). In contrast to the chlorido complex $\mathbf{1}^{+}$, $\mathbf{2}^{2+}$ exists in solution as a single *trans*-$\mathbf{2}^{2+}$ isomer according to NMR data (Figure S14), showing very similar spectra to those corresponding to *trans*-$\mathbf{1}^{+}$ given the fact that both molecules possess the same symmetry. The trans configuration of $\mathbf{2}^{2+}$ was also confirmed by X-ray diffraction analysis (see Figure 6a in the Comparative Analysis Section below), and the complex was further characterized by UV−vis spectroscopy (Figure S15a) and ESI-TOF MS (Figure S19a).

To prevent the isomeric equilibrium between the cis- and trans-chlorido forms and to obtain a single cis-aqua species to be compared to the *trans*-$\mathbf{2}^{2+}$ species (e.g., in catalysis), a methyl substituent was introduced at the 6′ position of one of the bpy moieties of bpy2PYMe to increase the steric hindrance and disrupt the formation of the trans configuration. The new ligand bpy(bpyMe)PYMe (L2, Chart 1) was obtained in a 17% yield following the same one-pot methodology used for the synthesis of bpy2PYMe (L1), the only difference being that 6-bromo-6′-methyl-2,2′-bipyridine was used instead of 6-bromo-2,2′-bipyridine (see Experimental Section for further details). A thorough NMR analysis of L2 can be found in Figure S16, in which the newly added methyl group can be clearly identified at 2.59 ppm in the HMBC spectrum. Concerning the respective chlorido and aqua complexes $\mathbf{3(Cl)}$ and $\mathbf{4(PF_6)_2}$, the synthetic strategy followed for their preparation is depicted in Scheme 1 and in the Experimental Section.

Complexes $\mathbf{3(Cl)}$ and $\mathbf{4(PF_6)_2}$ were characterized by NMR spectroscopy (Figures S17 and S18, respectively). The presence of 28 ^{13}C NMR resonances for $\mathbf{3(Cl)}$ and $\mathbf{4(PF_6)_2}$ and a ^{1}H NMR spectrum that resembles that of *cis*-$\mathbf{1}^{+}$ (although the signals now appear in a narrower range) are effectively an indication of the formation of a single cis isomer for both chlorido and aqua compounds. This is a consequence of the steric hindrance provided by the extra methyl group introduced into the original bpy2PYMe ligand (which according to the HMBC NMR spectra in Figures S17i and S18i can be assigned at 3.63 and 3.05 ppm for $\mathbf{3}^{+}$ and $\mathbf{4}^{2+}$, respectively). Moreover, the formation of a pure cis isomer for $\mathbf{3}^{+}$ and $\mathbf{4}^{2+}$ was also confirmed by X-ray diffraction analysis after slow evaporation of an acetone/water solution of $\mathbf{3(Cl)}$ (Figure S23, Table S2, and Experimental Section) and after ether diffusion into an acetone/DCM solution of $\mathbf{4(PF_6)_2}$ (see Figure 6b in the Comparative Analysis Section below). All Ru−N distances and N−Ru−N angles of both complexes logically resemble, and for *cis*-$\mathbf{3}^{+}$ the Ru−Cl distance (2.456 Å) lies within normal expected values.[7,13d,22]

Additionally, $\mathbf{3(Cl)}$ and $\mathbf{4(PF_6)_2}$ were characterized by ESI-TOF MS, UV−vis, and CV/differential pulse voltammetry (DPV) techniques (Figures S19, S21, and S22 in the Supporting Information, respectively), confirming the purity and integrity of the complexes and the expected similar spectroscopic and electrochemical properties to those of their related chlorido and aqua derivatives $\mathbf{1}^{+}$ and $\mathbf{2}^{2+}$, respectively. It should be highlighted as well that during the reductive scan of *cis*-$\mathbf{3}^{+}$ a $\mathbf{Ru^{II}\text{-}\kappa\text{-}N^{4}\text{-}bis\text{-}Cl}$ species is formed at potentials near 0.27 V (Figure S22a, black). However, this species cannot isomerize to a hypothetical *trans*-$\mathbf{3}^{+}$ species when reattaching the unbound N_{Pyr} ligand due to the steric hindrance introduced by the extra methyl group present in L2. We believe this is the

DOI: 10.1021/acs.inorgchem.6b01755
Inorg. Chem. XXXX, XXX, XXX−XXX

reason why no trace of either *trans*-$\mathbf{3}^{+}$ or *trans*-$\mathbf{4}^{2+}$ was detected. Furthermore, DFT calculations for both isomers of system **3** revealed that *cis*-$\mathbf{3}^{+}$ was 2.7 kcal/mol more stable than *trans*-$\mathbf{3}^{+}$, in perfect agreement with the experimental data.

Synthesis and Characterization of 5(Cl), 6(OTf)$_2$, 7(Cl), and 8(BF$_4$)$_2$. The synthetic strategy followed for the preparation of the respective chlorido and aqua complexes **5(Cl)** and **6(OTf)** bearing the PY5Me$_2$ (L3) ligand differs from the recently published data[7] and is therefore depicted in Scheme 3 and in the Experimental Section.

Scheme 3. Synthetic Pathway for the Preparation of the Chlorido Complexes $\mathbf{5}^{+}$ and $\mathbf{7}^{+}$ and the Aqua Complexes $\mathbf{6}^{2+}$ and $\mathbf{8}^{2+}$

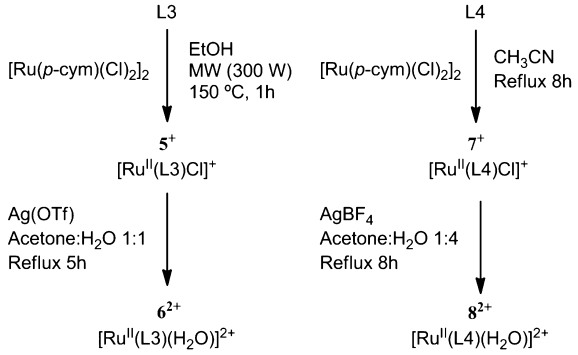

NMR spectra of $\mathbf{5}^{+}$and $\mathbf{6}^{2+}$ were coincident with data published by Kojima et al.[7] (for more information please refer to the Experimental Section), and good quality crystals of $\mathbf{6}^{2+}$ were obtained and analyzed by X-ray diffraction for the first time (Figures 6c and S24 and Table S4). Also, the electrochemical properties of $\mathbf{5}^{+}$ were studied by CV in acetonitrile (Figure S25), exhibiting a unique reversible wave at E^0 = 0.78 V versus SCE (ΔE = 61 mV), corresponding to the Ru^{III}/Ru^{II} process.

Complexes $\mathbf{7}^{+}$ and $\mathbf{8}^{2+}$, bearing the PY4Im (L4) ligand, were synthesized according to Scheme 3 (further details can be found in the Experimental Section) and were characterized by ESI-MS (Figures S26 and S27), NMR (Figures S28 and S29), CV and DPV (Figures S31–S33), and UV–vis (Figure S34) techniques. Compound $\mathbf{7}^{+}$ in MeOH shows a unique reversible wave at E^0 = 0.84 V (ΔE = 75 mV) corresponding to the Ru^{III}/Ru^{II} process (Figure S31). NMR analysis of $\mathbf{7}^{+}$ and $\mathbf{8}^{2+}$ shows that both compounds display C_{2v} symmetry in solution, with one symmetry plane passing through the chlorido/oxygen, the C(14) of the central imidazole, and the Ru atom and bisecting the C(12)–C(13) bond of the imidazole ring, thus interconverting the two sides of the complex. Moreover, one symmetry plane (perpendicularly bisecting the former) contains the imidazole ring and the Ru and chlorido/aqua groups, hence, interconverting the other two pyridine rings. As a result, we expect only six ^{1}H resonances, as confirmed in the corresponding ^{1}H NMR spectra (Figures S28a and S29a). It is worth mentioning that the characteristic downfield shift of the doublet corresponding to H1 (9.42 and 9.20 ppm, respectively) is likely due to hydrogen-bonding interactions between the protons α to the nitrogen atoms of each pyridyl ring and the chlorido/oxygen coordinated to the Ru ion. HMBC and HSQC experiments played an essential role in unambiguously assigning H12 and H6 singlets as well as all quaternary carbon resonances (Figures S28 and S29). Suitable crystals for X-ray diffraction analysis of **8**(BF$_4$)$_2$ were obtained as well (Figures 6d and S30 and Table S5), the structure of which is compared to those of *trans*-$\mathbf{2}^{2+}$, *cis*-$\mathbf{4}^{2+}$, and $\mathbf{6}^{2+}$ in the next Section.

Structural and Electrochemical Comparative Analysis of the Aqua Complexes. Mercury plots of the X-ray crystal structures of *trans*-$\mathbf{2}^{2+}$, *cis*-$\mathbf{4}^{2+}$, $\mathbf{6}^{2+}$, and $\mathbf{8}^{2+}$ are shown in Figure 6, and the corresponding crystallographic data can be found in Tables S1 and S3–S5, respectively. Table S6 includes a list of selected bond distances and angles for the four aqua complexes, which are in the expected range compared to other Ru(II) polypyridyl complexes.[23] The effect of the higher rigidity of the bpy2PYMe ligand (L1) compared to the more flexible PY5Me$_2$ (L3) and Py4Im (L4) ligands can be seen in the geometry around the Ru(II) atom, as it displays the least ideal octahedral environment of the series (N1–Ru–N2 and O–Ru–N$_5$ angles—entries 7 and 11—close to 170° and O–Ru–N1 angle—entry 12—close to 80° in *trans*-$\mathbf{2}^{2+}$, and longer Ru–N1 distance—entry 1—in *trans*-$\mathbf{2}^{2+}$ compared to $\mathbf{6}^{2+}$ and $\mathbf{8}^{2+}$). The distortion from the ideal octahedral geometry is even more pronounced upon introduction of the Me moiety to generate L2 (*cis*-$\mathbf{4}^{2+}$) due to the steric constraints it imposes. Thus, the N1–Ru–N3 and N2–Ru–N4 angles (entries 9 and 10) are 11° and 5° smaller than for the case of L1 (N1–Ru–N2 angle, entry 7), respectively, and the O–Ru–N1 and O–Ru–N4 angles are 12° and 6° off from 90° (entries 12 and 15 in Table S6, respectively, and Figure 6b).

On the one hand, the less rigid character of the L3 and L4 scaffolds is reflected in the relative orientation of the four equatorial pyridine rings in $\mathbf{6}^{2+}$ and $\mathbf{8}^{2+}$, which are clearly non parallel and show four α H atoms within hydrogen-bonding distance to the O atom of the aqua ligand (2.6–2.9 Å, Figure 6c,d). On the other hand, for L1 and L2 the existence of a C–C bridge in the bpy ligands precludes any relative rotation of the pyridine rings and impedes the approach of any pyridyl H atoms to the axial O atom. The closest distances for *trans*-$\mathbf{2}^{2+}$ fall in the range of 3.9 Å for O–H1, and they are in the range of 2.8 Å for O–H16 in *cis*-$\mathbf{4}^{2+}$ (Figure 6a,b), all of which are

Table 1. Redox Potentials at pH 7 (in V vs SCE), and pK_a Values for the Aqua-Complexes $\mathbf{2}^{2+}$, $\mathbf{4}^{2+}$, $\mathbf{6}^{2+}$, and $\mathbf{8}^{2+}$ and the Related Ru Complex [Ru(trpy)(bpy)(H$_2$O)]$^{2+}$

complex	III/II	IV/III	ΔE (mV)[d]	pK_{a1} (Ru^{III})	pK_{a2} (Ru^{II})	ref
trans-$\mathbf{2}^{2+}$ [a]	0.56	0.75	190	2.6	11.0	c
cis-$\mathbf{4}^{2+}$ [a]	0.51					c
$\mathbf{6}^{2+}$ [a]	0.38			2.7	10.7	c
$\mathbf{6}^{2+}$ [b]	0.46				11.0	7
$\mathbf{8}^{2+}$ [a]	0.58	0.80	220	5.3	12.7	c
[Ru(trpy) (bpy)(H$_2$O)]$^{2+}$ [a]	0.49	0.62	130	1.7	9.7	24

[a]In aqueous phosphate buffer pH 7. [b]In Britton–Robinson buffer. [c]This work. [d]$\Delta E = E^{IV/III} - E^{III/II}$.

DOI: 10.1021/acs.inorgchem.6b01755
Inorg. Chem. XXXX, XXX, XXX–XXX

longer than clear O···H bond distances. Exceptionally, one of the hydrogen atoms of the 6′ Me substituent in *cis*-$\mathbf{4}^{2+}$ lies within the limit of hydrogen bonding to the O atom (O−H28 distance of 2.6 Å), which is again an indication of the steric constraints imposed by the methylated ligand.

The last significant difference observed between the four structures is the shorter Ru−X_{ax} distance for $\mathbf{8}^{2+}$ (Table S6, entry 3) due to the much stonger σ-donor character of the carbene moiety (C_{ax}) with regard to the pyridyl scaffold present in *trans*-$\mathbf{2}^{2+}$, *cis*-$\mathbf{4}^{2+}$, and $\mathbf{6}^{2+}$. This feature has a dramatic effect in the acidity of the aqua group, which is significantly decreased (see pK_a values in Table 1 below). Interestingly, despite the presence of different coordinating atoms in the site trans to the aqua group, all Ru−O distances are similar, between 2.1 and 2.2 Å (Table S6, entry 6).

The electrochemical behavior of the aqua complexes was also studied in detail at different pH values, therefore allowing the construction of their Pourbaix diagrams (Figure S20), and a global comparison of the redox potentials at pH 7 and the pK_a values of *trans*-$\mathbf{2}^{2+}$, *cis*-$\mathbf{4}^{2+}$, $\mathbf{6}^{2+}$, $\mathbf{8}^{2+}$, and those of the paradigmatic Ru-penta-N-dentate complex[24] $[Ru(trpy)(bpy)(H_2O)]^{2+}$ (trpy = terpyridyne) is presented in Table 1.

It is well-known that the presence of an aqua group enables a simultaneous removal of electrons and protons (PCET) at relatively low and close potentials, since the buildup of high columbic charges is avoided,[25] allowing easy access to high oxidation states necessary for oxidative catalytic transformations. According to the Pourbaix diagrams (Figure S20), slopes of ca. −59 mV per pH unit in the central pH regions indicate the presence of the single PCET processes Ru^{III}−OH/Ru^{II}−OH_2 and Ru^{IV}−O/Ru^{III}−OH.[24] Consequently, the two waves observed at 0.56 and 0.75 V versus SCE for *trans*-$\mathbf{2}^{2+}$ and at 0.58 and 0.80 V for $\mathbf{8}^{2+}$ at pH 7 can be assigned to the Ru^{III}−OH/Ru^{II}−OH_2 and Ru^{IV}−O/Ru^{III}−OH processes, respectively (L1 and L4 were omitted for clarity), whereas for *cis*-$\mathbf{4}^{2+}$ and $\mathbf{6}^{2+}$ the wave corresponding to the Ru^{III}−OH/Ru^{II}−OH_2 process can be detected at 0.51 and 0.38 V, respectively (Table 1). Thus, at pH 7 the Ru^{III}/Ru^{II} and Ru^{IV}/Ru^{III} redox processes are separated by 190 mV in *trans*-$\mathbf{2}^{2+}$ and by 220 mV in $\mathbf{8}^{2+}$, while this separation is only of 130 mV in $[Ru^{II}(trpy)(bpy)]^{2+}$. This difference points out the higher stability of the Ru^{III}(OH) species of *trans*-$\mathbf{2}^{2+}$ and even more so for $\mathbf{8}^{2+}$ than in $[Ru^{II}(trpy)(bpy)]^{2+}$, which in the case of $\mathbf{8}^{2+}$ could be due to hydrogen-bonding interactions between the hydroxo group and the hydrogen atoms α to the pyridyl nitrogens of the pentadentate ligand (see Figure 6d).

Referring again to the Pourbaix diagrams, the two vertical lines (nonredox processes) allow determination of the pK_{a1} (Ru^{III}−OH_2) and pK_{a2} (Ru^{II}−OH_2) values. Therefore, for *trans*-$\mathbf{2}^{2+}$ these values are 2.6 and 11.0, respectively, which are very similar to those of $\mathbf{6}^{2+}$ (2.7 and 10.7) given the strong resemblance from an electronic viewpoint of L1 and L3. The pK_{a2} value for $\mathbf{6}^{2+}$ differs slightly from the value obtained previously by Kojima et al. (11.0),[7] although this difference may be attributed to the different buffers used in both works (Table 1). Finally, the pK_a values of the aqua group for $\mathbf{8}^{2+}$ (5.3 and 12.7 for Ru^{III} and Ru^{II}, respectively) are significantly higher because of the strong σ-donating character of the carbene scaffold present in L4. The decreased acidity of the aqua group in $\mathbf{8}^{2+}$ is also evident when comparing its pK_a values with those of $[Ru(trpy)(bpy)(H_2O)]^{2+}$; the p$K_{a1}$ and pK_{a2} values for the PY4Im complex increase by 3.6 and 3 units, respectively, compared to $[Ru(trpy)(bpy)(H_2O)]^{2+}$, while $\mathbf{2}^{2+}$ and $\mathbf{6}^{2+}$ occupy an intermediate position, with pK_a values only 0.9−1.3 units greater than those of $[Ru(trpy)(bpy)]^{2+}$.

Conclusions. The combined use of spectroscopic, spectrometric, electrochemical, and theoretical methods has led to a proposed isomerization mechanism for the $\mathbf{1}^{+}$ chlorido species and the quantification of the thermodynamic parameters. In MeOH both isomers are interconverted under thermal and photochemical conditions by a sequence of chlorido decoordination, decoordination/recoordination of a pyridyl group, and chlorido recoordination. Also, under oxidative conditions in DCM the exchange of a pyridyl group of the ligand by a Cl^- counterion in *trans*-$\mathbf{1}^{2+}$ generates a bis-chlorido intermediate $[Ru^{III}(\kappa\text{-}N^4\text{-bpy2PYMe})Cl_2]^+$ (**κ-N⁴-bis-Cl⁺**), which is essential for the isomerization process observed when the system is reduced back to Ru(II). In contrast, under the same conditions *cis*-$\mathbf{1}^{2+}$ is in direct equilibrium with *trans*-$\mathbf{1}^{2+}$, with absence of the **bis-Cl⁺** intermediate. Interestingly, its aqua derivative exists as a pure single isomer (*trans*-$\mathbf{2}^{2+}$), while by increasing the steric hindrance of the pentadentate ligand via introduction of a methyl group the isomerization equilibrium is completely inhibited, and a single cis isomer is obtained (*cis*-$\mathbf{3}^{+}$/*cis*-$\mathbf{4}^{2+}$). The electrochemical and structural data of this series of complexes ($\mathbf{1}^{+}$ to $\mathbf{4}^{2+}$) has also been compared to those of related Ru pentadentate chloro and aqua compounds, some of which are reported here for the first time ($\mathbf{7}^{+}$ and $\mathbf{8}^{2+}$). This comparison shows how the influence of the chemical and structural characteristics of the pentadentate ligand impacts the electrochemical and acid−base properties of the resulting Ru(II) complexes, which are fundamental for modulating their activity in redox catalysis. In the near future we plan to further extend this study by comparing the capacity of the aqua compounds described as catalysts for redox oxidative transformations.

EXPERIMENTAL SECTION

Materials. All reagents used in the present work were obtained from Aldrich Chemical Co. and were used without further purification. Reagent-grade organic solvents were obtained from Scharlab. $RuCl_3 \cdot 3H_2O$ and $[Ru(p\text{-cymene})(Cl)_2]_2$ were supplied by Alfa Aesar and were used as received. The synthesis of the ligand $PY5Me_2$ was performed following the procedure described in the literature.[26] To obtain the bpy2PYMe, bpy(bpyMe)PYMe, and PY4Im ligands, some modifications were introduced to the procedures already published. Thus, for bpy2PYMe[11] and bpy(bpyMe)PYMe we performed a one-pot reaction of 2-ethylpyridine with LDA and 6-bromo-2,2′-bipyridine (as well as 6-bromo-6′-methyl-2,2′-bipyridine for the latter), whereas for PY4Im[10] the silver derivative PY4Im-Ag was obtained by reaction of (PY4Im)Br with Ag_2O in acetonitrile instead of DCM (see Results Section for further details). All synthetic manipulations were routinely performed under nitrogen or argon atmosphere using Schlenk tubes and vacuum-line techniques.

Instrumentation and Measurements. UV−vis spectroscopy was performed by an HP8453 spectrometer using 1 cm quartz cells. NMR spectroscopy was performed on a Bruker DPX 250 MHz, DPX 360 MHz, DPX 400 MHz, or a DPX 600 MHz spectrometer. Samples were run in $CDCl_3$, MeOD, CD_3CN, CD_3NO_2, or acetone-d_6 with internal references. ESI-MS experiments were performed on an HP298s gas chromatography (GC-MS) system from the Servei d'Anàlisi Química of the Universitat Autònoma de Barcelona. MALDI-TOF MS measurements were run on a Bruker MALDI TOF ultrafleXtrem model under reflector mode by depositing on a GrounSteel plate 0.5 μL of a MeOH solution of the complexes. CV, DPV, and CPE experiments were performed on a Biologic SP-150 potentiostat, using EC Lab software for data acquisition and data handling. Measurements were made using a three-electrode conical cell equipped with a methanol jacket, which makes it possible to fix the temperature by

DOI: 10.1021/acs.inorgchem.6b01755
Inorg. Chem. XXXX, XXX, XXX−XXX

means of a thermostat. A glassy carbon disk electrode of 1.0 mm diameter (or a carbon graphite rod in the case of CPE) was used as a working electrode, a Pt disk of 1 mm diameter as an auxiliary electrode, and an aqueous SCE as a reference electrode. All of the potentials are reported versus SCE isolated from the working electrode compartment by a salt bridge. The salt solution of the reference calomel electrode is separated from the electrochemical solution by a salt bridge capped with a frit, which is made of a ceramic material, allowing ionic conduction between the two solutions and avoiding appreciable contamination. Ideally, the electrolyte solution present in the bridge is the same as the one used for the electrochemical solution, to minimize junction potentials. Working electrodes were polished with 0.05 μm alumina paste washed with distilled water and acetone before each measurement. The complexes were dissolved in acetone, acetonitrile, or DCM containing the necessary amount of n-Bu_4NPF_6 ($TBAPF_6$) or $TBABF_4$ as supporting electrolyte to yield 0.1 M ionic strength solutions. CV were recorded at a 100 mV·s^{-1} scan rate, and DPV were recorded using pulse amplitudes of 0.05 V, pulse widths of 0.05 s, sampling widths of 0.02 s, pulse periods of 0.1 s, and quiet times of 2 s. E^0 values reported in this work were estimated from CV experiments as the average of the oxidative and reductive peak potentials $(E_{p,a} + E_{p,c})/2$. The error associated with the potential values is less than 5 mV. To minimize the ohmic drop effects, the electrode used as a working electrode is 1.0 mm diameter, and the scan rates investigated were in the range of 0.1−1 V s^{-1}. Positive feedback iR compensation was used throughout. Typically compensated resistances were 0.5−2.0 kΩ, depending on the electrode location in the electrochemical cell. For the Pourbaix diagrams, CV and DPV of the corresponding aqua complexes were recorded in aqueous phosphate solutions to which small amounts of HCl 0.1 M or NaOH 0.1 M had been added to adjust the pH to the desired value. For the CPE experiments, a 0.68 mM solution of **1**(Cl) in 5 mL of DCM, containing 0.1 M of $TBAPF_6$ as supporting electrolyte, was prepared. Oxidative CPE at different potentials versus SCE was performed using a carbon graphite rod as a working electrode. After the passage of the desired number of faradays, the electrolysis was stopped, and the mixture was then analyzed by CV. For the light-induced isomerization processes, the dissolved complexes in a N_2-purged Schlenk flask were kept at 0 °C (water bath) and irradiated by a 100 W incandescent white light bulb, while for the temperature-driven isomerization processes the water bath was set at 50 °C and the Schlenk was covered with aluminum foil.

Computational Details. DFT calculations were performed with the Gaussian 09 set of programs.[27] For geometry optimizations, the well-established and computationally fast hybrid-GGA functional B3LYP was used,[28] including the D3 dispersion correction of Grimme.[29] The electronic configuration of the molecular systems was described with the standard split-valence basis set with a polarization function of Ahlrichs and co-workers for H, C, N, O, and Cl (SVP keyword in Gaussian).[30] For Ru we used the small-core, quasi-relativistic Stuttgart/Dresden effective core potential, with an associated valence basis set contracted (standard SDD keywords in Gaussian 09).[31−33] The geometry optimizations were performed without symmetry constraints, and the characterization of the located stationary points was performed by analytical frequency calculations.

Gibbs energies ΔG were built through single-point energy calculations on the B3LYP-d3/SVP geometries using the B3LYP-d3 functional and the triple-ζ valence plus polarization on main-group atoms (TZVP keyword in Gaussian).[34] Furthermore, diffuse basis sets (D95+) were incorporated for Cl.[35] Solvent effects were included with the Polarizable Continuum Model (PCM) using dichloromethane and methanol as solvents.[36] To these B3LYP-d3/TZVP electronic energies in solvent, zero-point energy and thermal and entropic corrections were included from the gas-phase frequency calculations at the B3LYP-d3/SVP level of theory.

Synthetic Preparations. *[Ru^{II}(bpy2PYMe)Cl]Cl [**1**(Cl)].* A sample of bpy2PYMe (0.140 mmol) was dissolved in 5 mL of dry ethanol, and then 81 mg of $[Ru(p\text{-cymene})(Cl)_2]_2$ (0.140 mmol) was added. The mixture was stirred and heated with a microwave (MW; 300 W) at 150 °C during 1 h. After this time the solution was filtrated through diatomaceous earth, and the volume was reduced in the rotary evaporator. After addition of ethanol, the *trans*-**1**(Cl) isomer precipitated as a burgundy colored solid, which was filtered and washed with DCM. Further addition of DCM to the supernatant yielded a burgundy colored solid (*cis*-**1**(Cl) isomer), which was filtered and washed with Et_2O. Yield: 20 mg (*trans*-**1**(Cl), 24%) and 49 mg (*cis*-**1**(Cl), 60%). ^{1}H NMR *cis*-**1**$^+$ (600 MHz, d_3-nitromethane, 298 K): δ = 9.93 (d, 1H, J19−18 = 4.9 Hz, H19), 9.27 (dd, 1H, J1−2 = 5.7 Hz, J1−3 = 1.1 Hz, H1), 8.54 (d, 1H, J16−17 = 7.5 Hz, H16), 8.31 (d, 1H, J12−11 = 8.0 Hz, H12), 8.26 (m, 2H, H17, H15), 8.21 (d, 1H, J13−14 = 7.5 Hz, H13), 8.17 (dd, 1H, J5−6 = 5.5 Hz, J5−7 = 2.1 Hz, H5), 8.13 (t, 1H, J14−13,15 = 7.9 Hz, H14), 8.08(d, 1H, J9−10 = 8.3 Hz, H9), 8.04 (m, 1H, H18), 7.95 (m, 2H, H6, H7), 7.92 (m, 1H, H10), 7.86 (t, 1H, J2−1,3 = 7.9 Hz, H2), 7.28 (t, 1H, J3−2,4 = 6.1 Hz, H3), 7.24 (t, 1H, J11−12,10 = 6.1 Hz, H11), 7.18 (d, 1H, J4−3 = 5.3 Hz, H4), 2.964 (s, 1H, H8). ^{13}C{^{1}H} NMR (151 MHz, d_3-nitromethane, 298 K): δ = 161.8 (C6), 160.1 (C5), 160.0 (C22), 159.5 (C23), 158.3 (C13), 158.0 (C10), 156.9 (C18, C1), 153.2 (C27), 152.1 (C4), 139.1 (C15), 138.2 (C25) 137.6 (C2), 136.3 (C8), 135.9 (C20), 128.6 (C26), 126.2 (C3), 124.7 (C24), 124.6 (C14), 124.4−124.3 (C9, C16), 123.5 (C17), 123.2 (C21), 122.8 (C13), 122.2 (C7) 59.8 (C11), 21.9 (C12). UV/vis (DCM): λmax, nm (ε, M^{-1}·cm^{-1}) = 295 (20517), 355 (5437), 523 (4496). ESI-MS (DCM): m/z = 552.1([M-Cl]$^+$). Elemental analysis (% found): C, 55.27; H, 3.67; N, 11.90. Calcd for $C_{27}H_{21}Cl_2N_5Ru$: C, 55.20; H, 3.60; N, 11.92. ^{1}H NMR *trans*-**1**$^+$ (400 MHz, d_3-nitromethane, 298 K): δ = 9.96 (d, 2H, J1−2 = 5.3 Hz, H1), 9.14 (d, 1H, J11−12 = 4.8 Hz, H12), 8.36 (d, 2H, J4−3 = 8.0 Hz, H4), 8.22 (dd, 2H, J7−6 = 6.4 Hz, J7−5 = 2.4 Hz, H7), 8.12 (m, 6H, H3,H5,H6), 7.90 (d, 1H, J9−10 = 8.1 Hz, H9), 7.83 (m, 3H, H2, H10), 7.08 (t, 1H, J11−10 = 6.3 Hz, J11−12 = 4.9 Hz, H11), 2.97 (s, 3H, H8). ^{13}C{^{1}H} NMR (100 MHz, d_3-nitromethane, 298 K): δ = 161.4 (C10), 160.9 (C6), 160.4 (C5), 157.4 (C17), 154.3 (C1), 140.9 (C13), 139.5 (C15) 139.1 (C3), 137.1 (C7), 126.6 (C2), 125.6 (C14), 124.3 (C16), 123.8 (C4), 122.7 (C8), 122.1 (C9), 60.8 (C11), 21.9 (C12). UV/vis (DCM): λmax, nm (ε, M^{-1}·cm^{-1})= 298 (19 198), 390 (4652), 534 (5029). ESI-MS (DCM): m/z = 552.1 ([M-Cl]$^+$). Elemental analysis (% found): C, 55.31; H, 3.68; N, 11.88. Calcd for $C_{27}H_{21}Cl_2N_5Ru$: C, 55.20; H, 3.60; N, 11.92.

*[Ru^{II}(bpy2PYMe)(H_2O)](PF_6)$_2$ [**2**(PF_6)$_2$].* An aliquot of 40 mg (0.06 mmol) of the 3:7 *trans*-**1**$^+$/*cis*-**1**$^+$ mixture obtained in the crude of the synthesis of **1**(Cl) was dissolved in 20 mL of water. The mixture was stirred and heated at 100 °C for 2 d, after which 0.5 mL of a NH_4PF_6 saturated aqueous solution was added. The volume was reduced until a brown precipitate appeared, which was filtered and washed with Et_2O. Yield: 43 mg (76%). ^{1}H NMR (400 MHz, d_6-acetone/D_2O 95:5, 298 K): δ = 10.32 (d, 2H, J1−2 = 5.4 Hz, H1), 9.58 (d, 1H, J12−11 = 4.7 Hz, H12), 8.84 (d, 2H, J4−3 = 8.0 Hz, H4), 8.70 (d, 2H, J7−6 = 7.3 Hz, H7), 8.51 (m, 7H, H3,H5,H6), 8.20 (m, 3H, H2, H9, H10), 7.50 (t, 1H, J11−10 = 6.4 Hz, J11−12= 4.9 Hz, H11), 3.21 (s, 3H, H8). ^{13}C{^{1}H} NMR (100 MHz, d_6-acetone/D_2O 95:5, 298 K): δ = 159.7 (C10), 159.4 (C6), 158.1 (C5), 157.2 (C13), 156.2 (C17), 154.5 (C1), 140.4 (C15) 140.0 (C3), 138.9 (C7), 127.4 (C2), 126.9 (C14), 124.7 (C16), 124.5 (C4), 123.8 (C8), 122.4 (C9), 59.9 (C11), 21.2 (C12). UV/vis (H_2O): λmax, nm (ε, M^{-1}·cm^{-1}) = 371 (3988), 494 (4485). ESI-MS (MeOH): m/z = 536.2 ([M-2PF_6-2H$^+$]$^+$). Elemental analysis (% found): C, 39.42; H, 2.85; N, 8.51. Calcd for $C_{27}H_{23}F_{12}N_5OP_2Ru$: C, 39.33; H, 2.81; N, 8.49.

bpy(bpyMe)PYMe (L2). For the synthesis of L2 the same methodology used for the synthesis of L1 was employed, except that in the second step (16 h reaction) 6-bromo-6′-methyl-2,2′-bipyridine was used instead of 6-bromo-2,2′-bipyridine. The synthesis of 6-bromo-6′-methyl-2,2′-bipyridine was performed introducing some modifications with respect to the procedure described in the literature.[37] Thus, to a solution of 2-bromo-6-methylpyridine in tetrahydrofuran (THF) at −65 °C, 1.2 equiv of BuLi in hexanes was added slowly (30 min), and the mixture was stirred for 3 h at −65 °C. Then, 1.2 equiv of Me_3SnCl in THF was added slowly (30 min), and the mixture was then allowed to slowly reach RT (1 h) under an Ar atmosphere and with constant stirring. The reaction was quenched with 10 mL of NH_4Cl saturated solution, and the mixture was

DOI: 10.1021/acs.inorgchem.6b01755
Inorg. Chem. XXXX, XXX, XXX−XXX

extracted with ethyl acetate and dried with sodium sulfate, filtered, and dried by solvent evaporation. The orange liquid obtained corresponds to 2-methyl-6-(trimethylstannyl)pyridine. Then, this stannate derivative was used to perform the coupling reaction with 2,6-dibromopyridine in the presence of LiCl (2 equiv) and $Pd(PPh_3)_4$ (catalytic amounts) to obtain 6-bromo-6′-methyl-2,2′-bipyridine, as described elsewhere.[38] Yield: 17%. ^{1}H NMR (400 MHz, $CDCl_3$, 298 K): δ = 8.62 (m, 2H), 8.30 (m, 2H), 8.26 (d, 1H, J = 7.3 Hz), 8.01 (d, 1H, J = 6.9 Hz), 7.71 (m, 3H), 7.54 (m, 2H), 7,15 (m, 6H), 2.59 (s, 3H), 2.54 (s, 3H). ^{13}C NMR (100 MHz, $CDCl_3$, 298 K): δ = 166.5, 165.2, 164.9, 157.5, 156.5, 155.9, 154.9, 154.5, 148.9, 148.7, 136.9, 136.7, 136.7, 136.7, 135.7, 123.9, 123.9, 123.6, 132.5, 123.5, 123.0, 121.3, 121.1, 118.3, 118.3, 118.2, 60.7, 27.7, 24.4. ESI-MS (DCM): m/z = 430.2 ([M + H]$^+$). Elemental analysis (% found): C, 78.21; H, 5.44; N, 16.34. Calcd for $C_{28}H_{23}N_5$: C, 78.30; H, 5.40; N, 16.31.

*[Ru^{II}(bpy(bpyMe)PYMe)Cl]Cl [**3**(Cl)].* A sample of bpy(bpyMe)-PYMe (0.233 mmol) was dissolved in 5 mL of dry ethanol, and then 71 mg of [Ru(p-cymene) $(Cl)_2]_2$ (0.116 mmol) was added. The mixture was stirred and heated with a MW (300 W) at 150 °C for 1 h. After this time the volume was reduced in the rotary evaporator. After addition of MeOH and 0.5 mL of a NH_4PF_6 saturated aqueous solution, *cis*-**3**(Cl) precipitated as a red solid, which was filtered and washed with MeOH and Et_2O. Yield: 112 mg (68%). ^{1}H NMR (400 MHz, d_2-DCM, 298 K): δ = 9.40 (d, 1H, J = 6.0 Hz), 8.33 (d, 1H, J = 8.0 Hz), 8.12 (m, 2H), 8.06 (m, 3H), 7.98 (m, 3H), 7.92 (t, 1H, J = 7.6 Hz), 7.83 (m, 3H), 7.31 (t, 1H, J = 6.4 Hz), 7.22 (t, 1H, J = 6.4 Hz), 6.90 (d, 1H, J = 6 Hz), 3.63 (s, 3H), 2.90 (s, 3H). ^{13}C NMR (100 MHz, d_2-DCM, 298 K): δ = 165.6, 161.2, 160.1, 159.0, 158.6, 158.6, 157.7, 156.9, 156.1, 150.6, 137.8, 137.3, 136.1, 135.9, 134.6, 128.3, 125.5, 123.2, 122.8, 122.7, 122.1, 122.0, 121.8, 121.7, 120.5, 57.8, 27.6, 21.9. UV/vis (DCM): λmax, nm (ε, M^{-1}·cm^{-1}) = 292 (29 954), 379 (4787), 502 (5802). ESI-MS (DCM): m/z = 566.1 ([M-Cl]$^+$). Elemental analysis (% found): C, 56.01; H, 3.89; N, 11.59. Calcd for $C_{28}H_{23}Cl_2N_5Ru$: C, 55.91; H, 3.85; N, 11.64.

*[Ru^{II}(bpy(bpyMe)PYMe)(H$_2$O)](PF$_6$)$_2$ [**4**(PF$_6$)$_2$].* An aliquot of 30 mg of **3**(Cl) was dissolved in 12 mL of water. The mixture was stirred and heated at 100 °C for 2 d, after which 0.5 mL of a NH_4PF_6 saturated aqueous solution was added. The volume was reduced until a red precipitate appeared, which was filtered and washed with Et_2O. Yield: 31 mg (86%). ^{1}H NMR (400 MHz, d_6-acetone/D_2O 5:95, 298 K): δ = 9.04 (d, 1H, J = 4.8 Hz), 8.27 (t, 2H, J = 7.6 Hz), 8.16 (dd, 1H, J = 6.8, 2.4 Hz), 8.01 (m, 6H), 7.81 (m, 5H), 7.28 (t, 1H, J = 6.4 Hz), 7.19 (t, 1H, J = 6.4 Hz), 7.02 (d, 1H, J = 6 Hz), 3.05 (s, 3H), 2.80 (s, 3H). ^{13}C NMR (100 MHz, d_6-acetone/D_2O 5:95, 298 K): δ = 164.2, 161.2, 158.7, 157.9, 157.0, 157.0 156.8, 156.5, 156.0, 151.7, 138.6, 138.2, 138.0, 136.7, 136.3, 128.7, 125.9, 124.2, 124.0, 123.7, 123.0, 122.5, 122.0, 121.4, 121.4, 58.0, 24.9, 20.5. UV/vis (H_2O): λmax, nm (ε, M^{-1}·cm^{-1}) = 300 (21 271), 354 (6125), 392 (5709), 521 (5203). ESI-MS (DCM): m/z = 550.1([M-2PF$_6$+2H]$^+$). Elemental analysis (% found): C, 40.19; H, 3.03; N, 8.32. Calcd for $C_{28}H_{25}F_{12}N_5OP_2Ru$: C, 40.11; H, 3.01; N, 8.35.

*[Ru^{II}(PY5Me$_2$)Cl]Cl [**5**(Cl)].* A sample of $PY5Me_2$ (0.225 mmol) was dissolved in 5 mL of dry ethanol, then 137 mg of [Ru(p-cymene) $(Cl)_2]_2$ (0.225 mmol) was added. The mixture was stirred and heated with a MW (300 W) at 150 °C during 1 h. After this time the volume was reduced in the rotary evaporator. After addition of Et_2O, a yellow solid precipitated, which was filtered and washed with Et_2O. Yield: 103 mg (74%). ^{1}H NMR (400 MHz, deuterated dimethyl sulfoxide (DMSO-d_6), 298 K) δ = 9.67 (dd, J = 5.8, 1.8 Hz, 4H), 8.04 (m, 7H), 7.96 (td, J = 7.8, 1.5 Hz, 4H), 7.53 (ddd, J = 7.3, 5.8, 1.4 Hz, 4H), 2.76 (s, 6H). Elemental analysis (% found): C, 56.66; H, 4.12; N, 11.31. Calcd for $C_{29}H_{25}Cl_2N_5Ru$: C, 56.59; H, 4.09; N, 11.38.

*[Ru^{II}(PY5Me$_2$)(H$_2$O)](OTf)$_2$ [**6**(OTf)$_2$].* **5**(Cl) (40 mg, 0.07 mmol) and AgOTf (23 mg, 0.09 mmol) were dissolved in darkness in a flask containing acetone/water (10 mL, 1:1). The resulting solution was stirred and heated under reflux for 5 h. After it cooled to room temperature, the solution was filtered to remove the AgCl byproduct. Slow evaporation of the acetone yielded a yellow solid, which was filtered and dried in air. The residue was crystallized by Et_2O diffusion into water. Yield: 40 mg (67%). ^{1}H NMR (400 MHz, DMSO-d_6, 298 K) δ = 9.45 (dd, J = 5.9, 1.7 Hz, 4H), 8.06 (m, 11H), 7.63 (ddd, J = 7.3, 5.7, 1.4 Hz, 4H), 7.52 (s, 2H), 2.78 (s, 6H). Elemental analysis (% found): C, 43.31; H, 3.19; N, 8.11. Calcd for $C_{31}H_{27}F_6N_5O_7S_2Ru$: C, 43.26; H, 3.16; N, 8.14.

PY4Im-Ag (L4). For the synthesis of L4, 2-methylpyridine reacted with 2-fluoropyridine via lithiation in hexanes affording 2-(2-pyridylmethyl)pyridine,[39] which was subsequently brominated to yield bis(2-pyridyl)bromomethane.[40] This precursor was then added to a basic solution containing imidazole to obtain (PY4Im)Br, as previously described by Long and Smith.[10] However, the silver derivative PY4Im-Ag could only be isolated as a pure white powder when (PY4Im)Br reacted with Ag_2O in acetonitrile instead of in CH_2Cl_2.[10]

*[Ru^{II}(PY4Im)Cl]Cl [**7**(Cl)].* [PY4ImAg]Br (0.062 g, 0.202 mmol) and [Ru(p-cymene) $(Cl)_2]_2$ (0.062 g, 0.101 mmol) were dissolved in a flask containing acetonitrile (25 mL), and the resulting solution was heated under reflux overnight. After that time a yellow precipitate appeared, which was filtered and dried with diethyl ether. Yield: 94 mg (86%).^{1}H NMR (400 MHz, DMSO-d_6, 298 K): δ = 9.42 (d, 4H, J1−2 = 5.67 Hz, H1), 7.93 (d, 4H, H4), 7.92 (t, 4H, H3), 7.77 (s, 2H, H12), 7.46 (t, 4H, H2), 7.45 (s, 2H, H6). ^{13}C{^{1}H} NMR (100 MHz, DMSO-d_6, 298 K): δ = 194.78 (C14), 155.63 (C1), 154.91 (C5), 137.20 (C4), 125.67 (C3), 124.40 (C2), 120.51 (C12), 65.19 (C6). ESI-MS (MeOH): m/z = 541.05([M-Cl]$^+$). Elemental analysis (% found): C, 52.10; H, 3.69; N, 14.51. Calcd for $C_{25}H_{21}Cl_2N_6Ru$: C, 52.00; H, 3.67; N, 14.55.

*[Ru^{II}(PY4Im)(H$_2$O)](BF$_4$)$_2$ [**8**(BF$_4$)$_2$].* **7**(Cl) (0.060 g, 0.103 mmol) and $AgBF_4$ (0.061 g, 0.309 mmol) were dissolved in darkness in a flask containing acetone/water (10 mL, 1:4). The resulting solution was stirred and heated under reflux overnight. After it cooled to room temperature, the solution was filtered to remove the AgCl byproduct. Slow evaporation of the acetone yielded yellow crystals, which were filtered and dried over air. Yield: 60 mg (84%). ^{1}H NMR (400 MHz, D_2O, 298 K): δ = 9.20 (d, 4H, J1−2 = 5.60 Hz, H1), 7.89 (d, 4H, H4), 7.87 (ddd, 4H, H3), 7.62 (s, 2H, H12), 7.44 (ddd, 4H, J2−3 = 7.73 Hz, J2−1 = 5.60 Hz, J2−4 = 2.12 Hz, H2), 7.13 (s, 2H, H6). ^{13}C{^{1}H} NMR (100 MHz, D_2O, 298 K): δ = 195.18 (C14), 154.24 (C1), 153.26 (C5), 137.15 (C4), 125.46 (C3), 124.00 (C2), 119.64 (C12), 66.07 (C6). UV/vis (aqueous solution at pH 8, phosphate buffer): λmax, nm (ε, M^{-1}·cm^{-1}) = 245 (10 270), 360 (6549), 394 (7140). ESI-MS (MeOH): m/z = 269.0 ([M-2BF$_4$−H$_2$O+MeOH]$^{2+}$). Elemental analysis (% found): C, 43.07; H, 3.35; N, 11.98. Calcd for $C_{25}H_{23}B_2F_8N_6ORu$: C, 43.01; H, 3.32; N, 12.04.

X-ray Crystal Structure Determination. X-ray crystal structure determination was made on a Bruker-Nonius diffractometer equipped with an APPEX II 4K CCD area detector, a FR591 rotating anode with Mo Kα radiation, Montel mirrors as a monochromatic, and a Kryoflex low-temperature device (T = −173 °C). Full-sphere data collection was used with w and f scans. Programs used were as follows: for data collection, Bruker APPEX II (versions v1.0−22, v2009.1−0 and v2009.1−02); for data reduction, Bruker SAINT (versions V.2.10, V/.60A and V7.60A); for absorption corrections, Bruker SADABS (versions V.2.10, V2008 and V2008/1);[41] and for structure refinement, SHELXTL (versions V6.12 and V6.14)[42] and SQUEEZE[43] implemented in Platon.[44]

Crystals of **2**$(PF_6)_2$ were obtained by slow ether diffusion in an acetone/water solution of the aqua complex. **2**$^{2+}$ crystallizes in a cell in which the asymmetric unit of this structure contains half a molecule of the cationic metal complex, which has C_s symmetry, since the Ru ion shows a distorted octahedral symmetry, two half PF_6^- anions, and highly disordered acetone molecules. The cationic metal complex is coordinated to an oxygen atom, which likely corresponds to a water molecule in accordance with the number of counteranions and a diamagnetic NMR spectrum. The PF_6^- anions are disordered in different orientations shared with neighboring asymmetric units. To avoid the highly disordered acetone molecules the program SQUEEZE[43] was applied leading to a refined model with an $R1$ value of 4.79% in which all the solvent molecules were removed. For **3**(**Cl**), crystals were obtained after slow evaporation of an acetone/water saturated solution of the chlorido complex. The asymmetric unit

DOI: 10.1021/acs.inorgchem.6b01755
Inorg. Chem. XXXX, XXX, XXX−XXX

of this structure contains one molecule of *cis*-3^{+} with distorted octahedral geometry, one Cl^{-} counterion, and seven water molecules, in agreement with a Ru(II) oxidation state. For $\mathbf{4}(\mathbf{PF_6})_2$, crystals were obtained after slow ether diffusion in an acetone/dichloromethane solution of the aqua complex. The asymmetric unit of this structure contains one molecule of *cis*-$\mathbf{4}^{2+}$ with distorted octahedral symmetry coordinated to a water molecule, two PF_6^{-} anions, and one dichloromethane molecule ($R1$ value of 3.02%). For $\mathbf{6}(\mathbf{OTf})_2$, crystals were obtained by slow ether diffusion in an acetone/water solution of the aqua complex. The structure of $\mathbf{6}^{2+}$ is very similar to that observed by Kojima for the corresponding chlorido complex,[7] containing a pseudo-octahedral coordination environment around the metal. Additionally, the triflate counterions appear above the coordinated water molecule within hydrogen-bonding distance, and the axial pyridine is tilted 3° from the $Ru-N_{ax}$ axis, similar to the observed 9° tilt for the Co(II) derivative of $Py5Me_2$.[8] For $\mathbf{8}(\mathbf{BF_4})_2$, crystals were obtained after slow evaporation of an acetone/water saturated solution of the aqua complex. $\mathbf{8}^{2+}$ crystallizes in a cell containing four $[Ru(PY4Im)(H_2O)]^{2+}$ cationic units, 16 water molecules, and eight BF_4^{-} anions, in agreement with a Ru(II) oxidation state. The asymmetric unit contains one molecule of the cationic complex with a coordinated water molecule, two BF_4^{-} anions, and four non-coordinated water molecules. One of the BF_4^{-} anions and three of the water molecules are disordered over two positions.

■ ASSOCIATED CONTENT

Supporting Information

The Supporting Information is available free of charge on the ACS Publications website at DOI: 10.1021/acs.inorgchem.6b01755.

Additional synthesis information, NMR, MALDI-TOF MS, and UV-vis spectra, light-induced isomerization process, CVs, energy diagrams, Mercury plot, Pourbaix diagram, tabulated crystallographic data, selected interatomic distances and angles, coordinates (PDF)

X-ray crystallographic information (ZIP)

■ AUTHOR INFORMATION

Corresponding Authors

*Fax: +34 93 581 24 77. E-mail: roger.bofill@uab.cat. (R.B.)

*E-mail: xavier.sala@uab.cat. Homepage: www.seloxcat.wordpress.com. (X.S.)

Notes

The authors declare no competing financial interest.

■ ACKNOWLEDGMENTS

Support from MINECO (CTQ2011-26440, CTQ-2016-80058-R, CTQ2014-59832-JIN, CTQ2015-69363-P, and CTQ2015-64261-R) is gratefully acknowledged. M.G.-S. is grateful for the award of a PIF doctoral grant from UAB. J.C.A. was supported by NSF-GRF Grant No. DGE-1106400. We deeply thank J. R. Long for his scientific advice and critical discussion and S. Gil-Moreno for the help in obtaining the crystals of $\mathbf{8}(BF_4)_2$.

■ REFERENCES

(1) Berardi, S.; Drouet, S.; Francàs, L.; Gimbert-Suriñach, C.; Guttentag, M.; Richmond, C.; Stoll, T.; Llobet, A. Molecular artificial photosynthesis. *Chem. Soc. Rev.* **2014**, *43*, 7501−7519.

(2) Bofill, R.; García-Antón, J.; Escriche, L.; Sala, X.; Llobet, A. *Comprehensive Inorganic Chemistry II* **2013**, *8*, 505−523.

(3) Chantarojsiri, T.; Sun, Y. J.; Long, J. R.; Chang, C. J. Water-Soluble Iron(IV)-Oxo Complexes Supported by Pentapyridine Ligands: Axial Ligand Effects on Hydrogen Atom and Oxygen Atom Transfer Reactivity. *Inorg. Chem.* **2015**, *54*, 5879−5887.

(4) (a) de Vries, M. E.; La Crois, R. M.; Roelfes, G.; Kooijman, H.; Spek, A.; Hage, R.; Feringa, B. L. A novel pentadentate ligand 2,6-bis[methoxybis(2-pyridyl)methyl]pyridine L for mononuclear iron(ii) and manganese(ii) compounds; synthesis and crystal structures of $[FeL(MeCN)][ClO_4]_2$ and $[(MnL(H_2O)][ClO_4]_2$. *Chem. Commun.* **1997**, 1549−1550. (b) Klein Gebbink, R. J. M.; Jonas, R. T.; Goldsmith, C. R.; Stack, T. D. P. A periodic walk: a series of first-row transition metal complexes with the pentadentate ligand PY5. *Inorg. Chem.* **2002**, *41*, 4633−4641.

(5) Wasylenko, D. J.; Ganesamoorthy, C.; Borau-Garcia, J.; Berlinguette, C. P. Electrochemical evidence for catalytic water oxidation mediated by a high-valent cobalt complex. *Chem. Commun.* **2011**, *47*, 4249−4251.

(6) (a) Goggins, E. M.; Lekich, T. T.; Weare, W. W.; Sommer, R. D.; Ribeiro, M. A.; Pinheiro, C. B. A Periodic Walk through a Series of First-Row, Oxido-Bridged, Heterodimetallic Molecules: Synthesis and Structure. *Eur. J. Inorg. Chem.* **2016**, *2016*, 1054−1059. (b) Zee, D. Z.; Chantarojsiri, T.; Long, J. R.; Chang, C. J. Metal−Polypyridyl Catalysts for Electro- and Photochemical Reduction of Water to Hydrogen. *Acc. Chem. Res.* **2015**, *48*, 2027−2036. (c) Wu, X. Y.; Huang, T.; Lekich, T. T.; Sommer, R. D.; Weare, W. W. Synthesis of Unsupported d^1-d^x Oxido-Bridged Heterobimetallic Complexes Containing V^{IV}: A New Direction for Metal-to-Metal Charge Transfer. *Inorg. Chem.* **2015**, *54*, 5322−5328. (d) King, A. E.; Nippe, M.; Atanasov, M.; Chantarojsiri, T.; Wray, C. A.; Bill, E.; Neese, F.; Long, J. R.; Chang, C. J. A Well-Defined Terminal Vanadium(III) Oxo Complex. *Inorg. Chem.* **2014**, *53*, 11388−11395. (e) Ghosh, S.; Singh, S. K.; Tewary, S.; Rajaraman, G. Enhancing the double exchange interaction in a mixed valence $\{V^{III}-V^{II}\}$ pair: a theoretical perspective. *Dalton Trans.* **2013**, *42*, 16490−16493. (f) Feng, X. W.; Liu, J. J.; Harris, T. D.; Hill, S.; Long, J. R. Slow Magnetic Relaxation Induced by a Large Transverse Zero-Field Splitting in a $Mn^{II}Re^{IV}(CN)_2$ Single-Chain Magnet. *J. Am. Chem. Soc.* **2012**, *134*, 7521−7529. (g) Zadrozny, J. M.; Freedman, D. E.; Jenkins, D. M.; Harris, T. D.; Iavarone, A. T.; Mathoniere, C.; Clerac, R.; Long, J. R. Slow Magnetic Relaxation and Charge-Transfer in Cyano-Bridged Coordination Clusters Incorporating $[Re(CN)_7]^{3-/4-}$. *Inorg. Chem.* **2010**, *49*, 8886−8896. (h) Freedman, D. E.; Jenkins, D. M.; Long, J. R. Strong magnetic exchange coupling in the cyano-bridged coordination clusters $[(PY5Me_2)_4V_4M(CN)_6]^{5+}$ (M = Cr, Mo). *Chem. Commun.* **2009**, 4829−4831. (i) Freedman, D. E.; Jenkins, D. M.; Iavarone, A. T.; Long, J. R. A Redox-Switchable Single-Molecule Magnet Incorporating $[Re(CN)_7]^{3-}$. *J. Am. Chem. Soc.* **2008**, *130*, 2884−2885.

(7) Ohzu, S.; Ishizuka, T.; Kotani, H.; Kojima, T. Reactivity of a Ru(III)−hydroxo complex in substrate oxidation in water. *Chem. Commun.* **2014**, *50*, 15018−15021.

(8) (a) Sun, Y.; Bigi, J. P.; Piro, N. A.; Tang, M. L.; Long, J. R.; Chang, C. J. Molecular Cobalt Pentapyridine Catalysts for Generating Hydrogen from Water. *J. Am. Chem. Soc.* **2011**, *133*, 9212−9215. (b) Sun, Y.; Sun, Y.; Long, J. R.; Yang, P.; Chang, C. J. Photocatalytic generation of hydrogen from water using a cobalt pentapyridine complex in combination with molecular and semiconductor nanowire photosensitizers. *Chem. Sci.* **2013**, *4*, 118−124.

(9) Karunadasa, H. I.; Chang, C. J.; Long, J. R. A molecular molybdenum-oxo catalyst for generating hydrogen from water. *Nature* **2010**, *464*, 1329−1333.

(10) Smith, J. M.; Long, J. R. First-Row Transition Metal Complexes of the Strongly Donating Pentadentate Ligand PY4Im. *Inorg. Chem.* **2010**, *49*, 11223−11230.

(11) Nippe, M.; Khnayzer, R. S.; Panetier, J. A.; Zee, D. Z.; Olaiya, B. S.; Head-Gordon, M.; Chang, C. J.; Castellano, F. N.; Long, J. R. Catalytic proton reduction with transition metal complexes of the redox-active ligand bpy2PYMe. *Chem. Sci.* **2013**, *4*, 3934−3945.

(12) (a) Weisser, F.; Hohloch, S.; Plebst, S.; Schweinfurth, D.; Sarkar, B. Ruthenium Complexes of Tripodal Ligands with Pyridine and Triazole Arms: Subtle Tuning of Thermal, Electrochemical, and Photochemical Reactivity. *Chem. - Eur. J.* **2014**, *20*, 781−793. (b) Weisser, F.; Stevens, H.; Klein, J.; van der Meer, M.; Hohloch, S.; Sarkar, B. Tailoring Ru^{II} Pyridine/Triazole Oxygenation Catalysts

DOI: 10.1021/acs.inorgchem.6b01755
Inorg. Chem. XXXX, XXX, XXX−XXX

and Using Photoreactivity to Probe their Electronic Properties. *Chem. - Eur. J.* **2015**, *21*, 8926−8938.
(13) (a) Francàs, L.; González-Gil, R.; Poater, X.; Fontrodona, X.; García-Antón, J.; Sala, X.; Escriche, L.; Llobet, A. Synthesis, Characterization, and Linkage Isomerism in Mononuclear Ruthenium Complexes Containing the New Pyrazolate-Based Ligand Hpbl. *Inorg. Chem.* **2014**, *53*, 8025−8035. (b) Vaquer, L.; Poater, A.; De Tovar, J.; García-Antón, J.; Solà, M.; Llobet, A.; Sala, X. Ruthenium Complexes with Chiral Bis-Pinene Ligands: an Array of Subtle Structural Diversity. *Inorg. Chem.* **2013**, *52*, 4985−4992. (c) Poater, A.; Mola, J.; Saliner, A. G.; Romero, I.; Rodríguez, M.; Llobet, A.; Solà, M. Mechanistic theoretical insight of Ru(II) catalysts with a meridional−facial bpea fashion competition. *Chem. Phys. Lett.* **2008**, *458*, 200−204. (d) Mola, J.; Romero, I.; Rodríguez, M.; Bozoglian, F.; Poater, A.; Solà, M.; Parella, T.; Benet-Buchholz, J.; Fontrodona, X.; Llobet, A. Mechanistic Insights into the Chemistry of Ru(II) Complexes Containing Cl and DMSO Ligands. *Inorg. Chem.* **2007**, *46*, 10707−10716.
(14) (a) McClure, B. A.; Abrams, E. R.; Rack, J. J. Excited State Distortion in Photochromic Ruthenium Sulfoxide Complexes. *J. Am. Chem. Soc.* **2010**, *132*, 5428−5436. (b) Sharma, R.; Knoll, J. D.; Martin, P. D.; Podgorski, I.; Turro, C.; Kodanko, J. J. Ruthenium Tris(2-pyridylmethyl)amine as an Effective Photocaging Group for Nitriles. *Inorg. Chem.* **2014**, *53*, 3272−3274.
(15) Santos, A. R.; Escudero, D.; González, L.; Orellana, G. Unravelling the Quenching Mechanisms of a Luminescent Ru^{II} Probe for Cu^{II}. *Chem. - Asian J.* **2015**, *10*, 622−629.
(16) Blancafort, L. Photochemistry and Photophysics at Extended Seams of Conical Intersection. *ChemPhysChem* **2014**, *15*, 3166−3181.
(17) Ding, L.; Chung, L. W.; Morokuma, K. J. Excited-State Proton Transfer Controls Irreversibility of Photoisomerization in Mononuclear Ruthenium(II) Monoaquo Complexes: A DFT Study. *J. Chem. Theory Comput.* **2014**, *10*, 668−675.
(18) The ferrocene/ferrocenium couple measured in DCM + 0.1 M of *n*-Bu_4NPF_6 is 0.509 (error 0.009) V versus SCE, which is in agreement with previous studies performed by N. G. Tsierkezos: Tsierkezos, N. G. Cyclic Voltammetric Studies of Ferrocene in Nonaqueous Solvents in the Temperature Range from 248.15 to 298.15 K. *J. Solution Chem.* **2007**, *36*, 289−302.
(19) (a) Savéant, J. M. *Elements of Molecular and Biomolecular Electrochemistry;* Wiley-Interscience: New York, 2006. (b) Bard, A. J. *Electrochemical Methods: Fundamentals and Applications;* John Wiley & Sons, Inc: New York, 2001.
(20) Bott, A. W.; Feldberg, S. W.; Rudolph, M. Fitting Experimental Cyclic Voltammetry Data with Theoretical Simulations Using DigiSim® 2.1. *Current Separations* **1996**, *15*, 2.
(21) Estimated errors in the equilibrium and kinetic constants using DigiSim are less than 10%.
(22) Mola, J.; Dinoi, C.; Sala, X.; Rodríguez, M.; Romero, I.; Parella, T.; Fontrodona, X.; Llobet, A. A new dinuclear Ru-Hbpp based water oxidation catalyst with a *trans*-disposition of the Ru-OH. *Dalton Trans.* **2011**, *40*, 3640−3646.
(23) (a) Zong, R.; Thummel, R. A New Family of Ru Complexes for Water Oxidation. *J. Am. Chem. Soc.* **2005**, *127*, 12802−12803. (b) Duan, L.; Fischer, A.; Xu, Y.; Sun, L. Isolated Seven-Coordinate Ru(IV) Dimer Complex with $[HOHOH]^-$ Bridging Ligand as an Intermediate for Catalytic Water Oxidation. *J. Am. Chem. Soc.* **2009**, *131*, 10397−10399. (c) Yagi, M.; Tajima, S.; Komi, M.; Yamazaki, H. Highly active and tunable catalysts for O_2 evolution from water based on mononuclear ruthenium(II) monoaquo complexes. *Dalton Trans.* **2011**, *40*, 3802−3804.
(24) Takeuchi, K. J.; Thompson, M. S.; Pipes, D. W.; Meyer, T. J. Redox and Spectral Properties of Monooxo Polypyridyl Complexes of Ruthenium and Osmium in Aqueous Media. *Inorg. Chem.* **1984**, *23*, 1845−1851.
(25) (a) Huynh, M. H. V.; Meyer, T. J. Proton-Coupled Electron Transfer. *Chem. Rev.* **2007**, *107*, 5004−5064. (b) Gagliardi, C. J.; Westlake, B. C.; Kent, C. A.; Paul, J. J.; Papanikolas, J. M.; Meyer, T. J. Integrating proton coupled electron transfer (PCET) and excited states. *Coord. Chem. Rev.* **2010**, *254*, 2459−2471.
(26) Bechlars, B.; D'Alessandro, D. M.; Jenkins, D. M.; Iavarone, A. T.; Glover, S. D.; Kubiak, C. P.; Long, J. R. High-spin ground states via electron delocalization in mixed-valence imidazolate-bridged divanadium complexes. *Nat. Chem.* **2010**, *2*, 362−368.
(27) Frisch, M. J.; Trucks, G. W.; Schlegel, H. B.; Scuseria, G. E.; Robb, M. A.; Cheeseman, J. R.; Scalmani, G.; Barone, V.; Mennucci, B.; Petersson, G. A.; Nakatsuji, H.; Caricato, M.; Li, X.; Hratchian, H. P.; Izmaylov, A. F.; Bloino, J.; Zheng, G.; Sonnenberg, J. L.; Hada, M.; Ehara, M.; Toyota, K.; Fukuda, R.; Hasegawa, J.; Ishida, M.; Nakajima, T.; Honda, Y.; Kitao, O.; Nakai, H.; Vreven, T.; Montgomery, J. A., Jr.; Peralta, J. E.; Ogliaro, F.; Bearpark, M.; Heyd, J. J.; Brothers, E.; Kudin, K. N.; Staroverov, V. N.; Kobayashi, R.; Normand, J.; Raghavachari, K.; Rendell, A.; Burant, J. C.; Iyengar, S. S.; Tomasi, J.; Cossi, M.; Rega, N.; Millam, J. M.; Klene, M.; Knox, J. E.; Cross, J. B.; Bakken, V.; Adamo, C.; Jaramillo, J.; Gomperts, R.; Stratmann, R. E.; Yazyev, O.; Austin, A. J.; Cammi, R.; Pomelli, C.; Ochterski, J. W.; Martin, R. L.; Morokuma, K.; Zakrzewski, V. G.; Voth, G. A.; Salvador, P.; Dannenberg, J. J.; Dapprich, S.; Daniels, A. D.; Farkas, Ö.; Foresman, J. B.; Ortiz, J. V.; Cioslowski, J.; Fox, D. J. *Gaussian 09,* Revision D.01; Gaussian, Inc: Wallingford, CT, 2009.
(28) (a) Becke, A. D. Density-functional thermochemistry. III. The role of exact exchange. *J. Chem. Phys.* **1993**, *98*, 5648−5652. (b) Lee, C.; Yang, W.; Parr, R. G. Development of the Colle-Salvetti correlation-energy formula into a functional of the electron density. *Phys. Rev. B: Condens. Matter Mater. Phys.* **1988**, *37*, 785−789. (c) Stephens, P.; Devlin, F. J.; Chabalowski, C. F.; Frisch, M. J. Ab Initio Calculation of Vibrational Absorption and Circular Dichroism Spectra Using Density Functional Force Fields. *J. Phys. Chem.* **1994**, *98*, 11623−11627.
(29) Grimme, S.; Ehrlich, S.; Goerigk, L. Effect of the damping function in dispersion corrected density functional theory. *J. Comput. Chem.* **2011**, *32*, 1456−1465.
(30) Schaefer, A.; Horn, H.; Ahlrichs, R. Fully optimized contracted Gaussian basis sets for atoms Li to Kr. *J. Chem. Phys.* **1992**, *97*, 2571−2577.
(31) Haeussermann, U.; Dolg, M.; Stoll, H.; Preuss, H.; et al. Accuracy of energy-adjusted quasirelativistic ab initio pseudopotentials: all-electron and pseudopotential benchmark calculations for Hg, HgH and their cations. *Mol. Phys.* **1993**, *78*, 1211−1224.
(32) Kuechle, W.; Dolg, M.; Stoll, H.; Preuss, H. Energy-Adjusted Pseudopotentials for the Actinides. Parameter Sets and Test Calculations for Thorium and Thorium Monoxide. *J. Chem. Phys.* **1994**, *100*, 7535−7542.
(33) Leininger, T.; Nicklass, A.; Stoll, H.; Dolg, M.; Schwerdtfeger, P. The accuracy of the pseudopotential approximation. II. A comparison of various core sizes for indium pseudopotentials in calculations for spectroscopic constants of InH, InF, and InCl. *J. Chem. Phys.* **1996**, *105*, 1052−1059.
(34) Weigend, F.; Ahlrichs, R. Balanced basis sets of split valence, triple zeta valence and quadruple zeta valence quality for H to Rn: Design and assessment of accuracy. *Phys. Chem. Chem. Phys.* **2005**, *7*, 3297−3305.
(35) Dunning, T. H., Jr; Hay, P. J. In *Modern Theoretical Chemistry;* Schaefer, H. F., III, Ed.; Plenum: New York, 1977; Vol. 3, pp 1−28.
(36) Marenich, A. V.; Cramer, C. J.; Truhlar, D. G. Universal Solvation Model Based on Solute Electron Density and on a Continuum Model of the Solvent Defined by the Bulk Dielectric Constant and Atomic Surface Tensions. *J. Phys. Chem. B* **2009**, *113*, 6378−6396.
(37) Bianchini, C.; Gatteschi, D.; Giambastiani, G.; Guerrero Rios, I.; Ienco, A.; Laschi, F.; Mealli, C.; Meli, A.; Sorace, L.; Toti, A.; Vizza, F. Electronic Influence of the Thienyl Sulfur Atom on the Oligomerization of Ethylene by Cobalt(II) 6-(Thienyl)-2-(imino)pyridine Catalysis. *Organometallics* **2007**, *26*, 726−739.
(38) Patroniak, V.; Kubicki, A.; Stefankiewicz, A. R.; Grochowska, A. M. V. Preparation of new heterotopic ligands. *Tetrahedron* **2005**, *61*, 5475−5480.

DOI: 10.1021/acs.inorgchem.6b01755
Inorg. Chem. XXXX, XXX, XXX−XXX

(39) Dyker, G.; Muth, O. Synthesis of Methylene- and Methine-Bridged Oligopyridines. *Eur. J. Org. Chem.* **2004**, *2004*, 4319−4322.
(40) Vedernikov, A. N.; Fettinger, J. C.; Mohr, F. Synthesis and Reactivity of Dimethyl Platinum(IV) Hydrides in Water. *J. Am. Chem. Soc.* **2004**, *126*, 11160−11161.
(41) Blessing, R. H. An empirical correction for absorption anisotropy. *Acta Crystallogr., Sect. A: Found. Crystallogr.* **1995**, *A51*, 33−38.
(42) Sheldrick, G. M. A short history of SHELX. *Acta Crystallogr., Sect. A: Found. Crystallogr.* **2008**, *A64*, 112−122.
(43) (a) van der Sluis, P.; Spek, A. L. BYPASS: an effective method for the refinement of crystal structures containing disordered solvent regions. *Acta Crystallogr., Sect. A: Found. Crystallogr.* **1990**, *A46*, 194−201. (b) Spek, A. L. PLATON SQUEEZE: a tool for the calculation of the disordered solvent contribution to the calculated structure factors. *Acta Crystallogr., Sect. C: Struct. Chem.* **2015**, *C71*, 9−18.
(44) Spek, A. L. Single-crystal structure validation with the program PLATON. *J. Appl. Crystallogr.* **2003**, *36*, 7−13.

DOI: 10.1021/acs.inorgchem.6b01755
Inorg. Chem. XXXX, XXX, XXX−XXX